The Cubic-Spline Transform Method: Basic Definitions and Tests in a 1D Single Domain

KATSUYUKI V. OOYAMA*

Hurricane Research Division, AOML, NOAA, Miami, Florida

(Manuscript received 4 September 2001, in final form 29 January 2002)

ABSTRACT

The purpose of the paper is to describe the technical details of a numerical method that combines the cubic-spline representation of spatial variables in a finite domain with the logistics of the spectral transform method for the time integration of nonlinear meteorological equations. The reason for developing the method lies in its application to two-way interacting nested models of the atmosphere. When compared with the gridpoint representation, the cubic-spline representation allows direct evaluation of derivatives in the model equations, and leads to a substantial reduction of shortwave dispersion of advecting and propagating waves. When compared with the Fourier spectral representation, the cubic B-splines as basis functions provide simple but exact means of implementing a variety of boundary conditions that are needed at the domain interfaces, as well as at natural boundaries. A sharp (sixth order) low-pass filter, which is built into the cubic-spline transform, effectively eliminates adverse nonlinear accumulation of small-scale errors near the resolution limit. These features, critically important to noise-free nesting, are defined and analyzed in this paper in the simpler context of a single 1D domain. The actual procedures for two-way interactive nesting will be presented in a subsequent paper.

1. Introduction

The purpose of the present paper is to describe the basic definitions and fundamental properties of a numerical method that combines the spatial representation of dependent variables by cubic splines with the logistics of the spectral transform method (Orszag 1970; Machenhauer 1979) for the time integration of nonlinear meteorological equations. While the essence of the method was described earlier in DeMaria et al. (1992), this paper offers a more refined and detailed account, including an error analysis.

Acknowledging its conceptual indebtedness to the spectral transform method, DeMaria et al. called the method the Spectral Application of Finite-Element Representation (SAFER), in which cubic B-splines on regularly spaced nodes are the finite elements. Cubic-spline functions are of second-order continuity, and the primitive-form meteorological equations are, at most, of second order. Thus, evaluation of the equations in physical space parallels the corresponding inverse leg of the spectral transform method. On the other hand, the projection of a given spatial function on a spline function is not a true spectral transform, since the B-spline basis is neither analytic nor orthogonal. In particular, the rate of global convergence of the cubic-spline representation is limited to the fourth order (see the appendix for detailed discussions), although, when compared in terms of shortwave dispersion, it is much more accurate than the sixth-order finite-difference method. Our use of the term *spectral* was not intended, as some critics interpreted, to suggest that the SAFER method was a conventional spectral method. In favor of noncontroversial terminology, our method will be called, below, the Cubic-Spline Transform (CST) method.

The reason for proposing the CST method lies in its application to nested models that may be employed, for example, in the simulation of mesoscale weather systems with explicitly resolved moist convection. It is computationally tempting to configure such a model on a sequence of nested domains of outwardly decreasing resolution. However, in solving the hyperbolic system of meteorological equations for a nonhydrostatic compressible atmosphere, the domains must communicate with each other by means of propagating waves and material advection. Since an early exploration by Phillips and Shukla (1973), the strategy of nesting for gridpoint models has progressed, through the related problems of open boundary and one-way nesting for a finite domain (Orlanski 1976; Miyakoda and Rosati 1977;

* Current affiliation: Cooperative Institute for Marine and Atmospheric Studies, Rosenstiel School for Marine and Atmospheric Science, University of Miami, Miami, Florida.

Corresponding author address: Katsuyuki V. Ooyama, Hurricane Research Division, AOML, NOAA, 4301 Rickenbacker Cswy., Miami, FL 33149-1097.
E-mail: Vic.Ooyama@noaa.gov

Miller and Thorpe 1981), to the present, practical levels of two-way nesting of multiple domains (Zhang et al. 1986; Chen 1991; Grell et al. 1995). In these and many other similar works, one of the major concerns is the reduction of numerical noise that propagating and advecting waves generate at domain interfaces. The noise can be suppressed by various means, but only with a severe reduction of the actual spectral range (bandwidth) within which remaining signals participate in the communication.

By adopting a nesting strategy, we accept the obvious fact that certain short waves in one domain are geometrically unresolvable in another of a coarser resolution. No numerical scheme can alter this fact. However, it must also be recognized that even would-be-resolvable waves are not necessarily transmissible to the coarse domain. Transmissibility depends on dynamics and is determined by the existence of a matching time frequency on both sides of the interface. It can be improved by accurate numerical schemes though not beyond the limit of resolvability. In this regard, those grid-point models, which are commonly based on second-order finite-difference schemes for spatial derivatives, fall far short of the ideal limit of transmissibility, due to their broad spectral extent of computational dispersion. Higher-order finite-difference schemes reduce the dispersion but complicate the formulation of interface conditions. The Fourier spectral method eliminates dispersion but is applicable only to a single periodic domain.[1] The CST method is an attempt to combine the versatility of cubic splines in setting boundary/interface conditions with the numerical accuracy of the Fourier spectral transform method for reduced dispersion.

The performance of the CST method in 2D nested models has been demonstrated by Shapiro and Ooyama (1990), DeMaria et al. (1992), and Ooyama (2001). In the present paper, however, the method is discussed only in the simple context of a 1D single domain, in order to establish the formalism and characteristic properties of the method that are to be exploited in the development of nesting strategies. Thus, the basic definitions of the cubic-spline representation, boundary conditions, and transforms are discussed in sections 2 through 4; the built-in low-pass filter in section 5; the logistic design of the application to prognostic models in section 6; applications to linear and nonlinear advection equations in sections 7 and 8; and tests of outgoing advective and propagating waves through open boundaries in section 9. The discretization error near the Nyquist scale, as well as the global convergence rate of the representation, is discussed in the appendix. The actual procedures of two-way nesting will be presented in a supplemental paper.

It is noted that finite elements have been employed in numerical models in various contexts. In semi-Lagrangian models (e.g., Staniforth and Côté 1991), cubic splines are used as one of the interpolation schemes. (We adhere to the Eulerian form of time integration, since moist processes involving abrupt phase changes are not amenable to the Lagrangian promise of a large time step.) Applications were also made of finite elements, especially the linear B-spline (usually in the Galerkin method), to the Eulerian integration of hyperbolic problems. On the basis of his general error analysis, however, Cullen (1979) concluded that finite-element approximations did not lead to very accurate schemes considering their computational cost, except for special cases that needed to be identified. We believe that the proposed transform method with cubic splines, which was not in the categories Cullen examined, is very accurate and versatile, although it is not a paragon of computational economy.

2. Spatial representation of variables by cubic splines

a. The domain, nodes, and basis functions

A one-dimensional domain D is defined as a closed interval in x with end points x_O and $x_{O'}$. The domain is divided into $\overline{m}$ subintervals of equal size Δx. The dividing points, including the two end points, will be called *nodes* and the subintervals *nodal cells*. In addition, two extra nodes are defined outside D, each Δx away from x_O or $x_{O'}$. In a formal notation, we write

$$\begin{aligned} D &= \{x \,|\, x_O \le x \le x_{O'}\}, \\ M &= \{-1, 0, 1, \ldots, \overline{m}, \overline{m}+1\}, \\ \Delta x &= (x_{O'} - x_O)/\overline{m}, \\ x_m &= x_O + m\Delta x \quad \text{for } m \in M, \end{aligned} \tag{2.1}$$

where M is the set of all the nodal indices and x_m is any one of $\overline{m}+3$ nodes; in particular, x_{-1} and $x_{\overline{m}+1}$ are the nodes outside D. The set of these discrete nodes may be referred to as the *mesh* and the continuous interval D as the *domain*, although the two terms are nearly interchangeable unless the two extra nodes really matter in a particular context.

In terms of the normalized coordinate ξ, the cubic B-spline $\Phi(\xi)$ may be defined by

$$\Phi(\xi) = \begin{cases} \dfrac{1}{6}(1-|\xi|)^3 - \dfrac{2}{3}(1-|\xi|)^3 & \text{if } 1 \ge |\xi| \ge 0, \\ \dfrac{1}{6}(2-|\xi|)^3 & \text{if } 2 \ge |\xi| \ge 1, \\ 0 & \text{if } |\xi| \ge 2. \end{cases} \tag{2.2}$$

[1] Although certain spectral methods can accommodate arbitrary boundary conditions, they are not suitable to two-way nesting on multiple domains. For example, the modified Fourier spectral method (Juang and Kanamitsu 1994) is designed only for one-way nesting. When Chebyshev's or Legendre's polynomials are used as the spectral basis (Gottlieb and Orszag 1977; Fulton and Schubert 1987), the spatial resolution is variable within a domain and skewed toward the boundaries, while inward refinement of resolution is expected of nested atmospheric models.

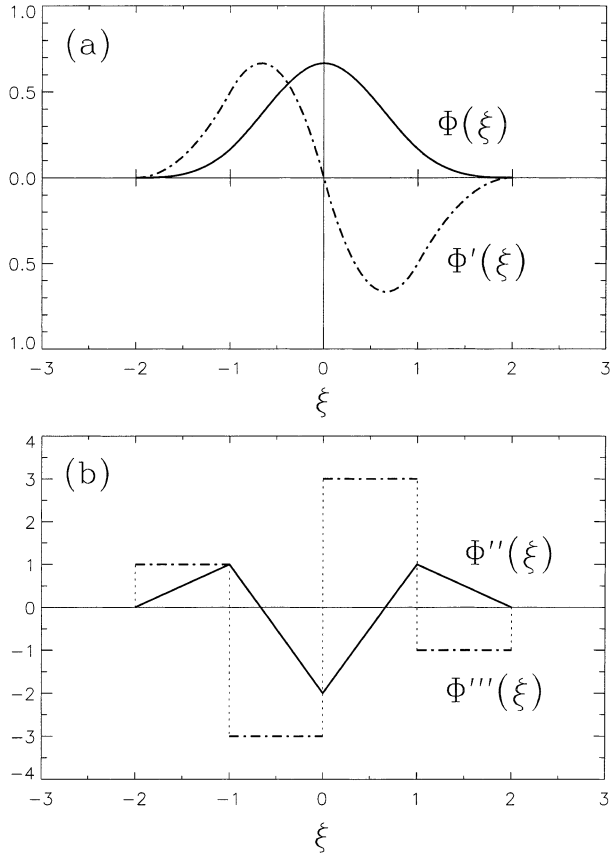

FIG. 1. (a) The cubic B-spline Φ on the normalized abscissa ξ and its first derivative; (b) the second and third derivatives.

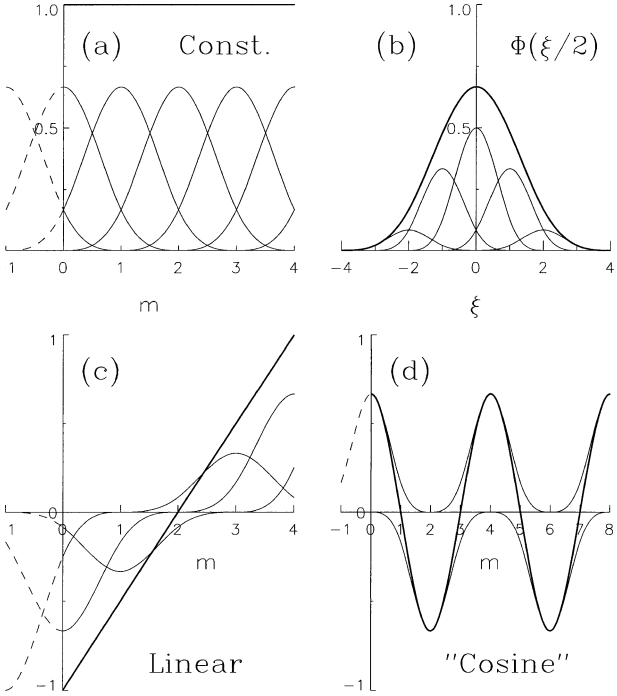

FIG. 2. Simple examples of cubic-spline functions (thick lines) in S_3: (a) a constant (unity), (b) a double-width B-spline, (c) a straight line, and (d) a $4\Delta x$ cosine (approximate; see Fig. A2 for the parasitic error). Thin lines are contributing members of nodal splines.

As shown in Fig. 1, the four nontrivial segments of cubic polynomials constitute a finite element of second-order continuity. Its third-order derivative is piecewise continuous and integrable. Note that (2.2) differs by the factor 2/3 from a similar definition in DeMaria et al. (1992).

In order to form the basis of field representation in D, a basis function $\phi_m(x)$ is assigned to each node x_m, such that

$$\phi_m(x) = \Phi\left(\frac{x - x_m}{\Delta x}\right), \quad \text{for } m \in M \quad \text{and} \quad x \in D. \quad (2.3)$$

If $x \notin D$, $\phi_m(x)$ should be considered undefined. The numerical magnitude of (2.2) has been chosen to normalize the sum,

$$\sum_{m \in M} \phi_m(x) = 1, \quad \text{for } x \in D. \quad (2.4)$$

Although generalized definitions of B-splines on irregular nodes are possible (de Boor 1987), the above with equally spaced nodes is the most suitable for our model of hyperbolic equations, since every nodal cell has an equal ability to represent propagating waves.

b. *The class of cubic-spline functions*

The ordered set of $(\overline{m} + 3)$ basis functions (2.3) may be denoted as the column vector,

$$\boldsymbol{\phi} = [\phi_m(x)]^{\mathrm{T}}_{m \in M} = [\phi_{-1}, \ldots, \phi_m, \ldots, \phi_{\overline{m}+1}]^{\mathrm{T}}. \quad (2.5)$$

Then, for any ordered set of $(\overline{m} + 3)$ scalar amplitudes a_m, also denoted as a column vector,

$$\mathbf{a} = [a_m]^{\mathrm{T}}_{m \in M} = [a_{-1}, \ldots, a_m, \ldots, a_{\overline{m}+1}]^{\mathrm{T}}, \quad (2.6)$$

the linear form,

$$u(x) = \boldsymbol{\phi}^{\mathrm{T}}\mathbf{a} = \sum_{m \in M} \phi_m(x) a_m, \quad (2.7)$$

defines a cubic-spline function $u(x)$. It is important to note that $u(x)$ is defined only in the closed domain D, and that, even though numerical values can be assigned to (2.7) for $x \notin D$, they are meaningless by definition and should never be used.

For the set of all possible vectors $\mathbf{a}$, the collection (2.7) defines the class of cubic-spline functions S_3. A few examples of simple members are illustrated in Fig. 2. The curve in Fig. 2d, labeled "cosine," is approximate but the others are as exact as labeled. In particular, the fact that the double-width B-spline $\Phi(\xi/2)$ in Fig. 2b belongs to S_3 is significant when we later consider the basis conversion between nested domains of different Δx.

An obvious disadvantage of the B-spline basis is the lack of global orthogonality. Since an orthogonal set of new basis functions can be constructed from linear combinations of $\phi_m(x)$, the nonorthogonality is not absolute; the reconstructed orthogonal basis, however, will destroy the style and practicality of cubic-spline transforms (section 4). On the other hand, the model application of (2.7) requires $u(x)$ to satisfy certain boundary conditions (BCs). Since BCs are local properties, their implementation is greatly facilitated by the locally defined $\phi_m(x)$.

3. Boundary conditions

a. The rank and type of boundary conditions

Except for global models that have no lateral boundary, the domain boundaries in atmospheric models are usually artificial assumptions for convenience. Thus, in addition to those conditions that reflect real physical requirements (e.g., at the earth's surface), it is also necessary to consider those BCs whose purpose is to restore or emulate, as much as possible, the lost reality due to modeling assumptions. Therefore, our discussion, below, includes every possible set of BCs that defines a subclass of S_3. The choice of appropriate sets of BCs is an important but somewhat heuristic problem of modeling, and has to be decided in specific applications.

Since $u(x) \in S_3$ and its first two derivatives are defined at x_O, as many as three independent conditions of the form

$$c_0 u(x_O) + c_1 u'(x_O) + c_2 u''(x_O) = g \qquad (3.1)$$

may simultaneously be imposed as a set on $u(x)$, where c_0, c_1, c_2, and g are given constants; if $g = 0$, the condition is homogeneous, and otherwise inhomogeneous. The total number of independent conditions in such a set is called the rank and is denoted by r, while the coefficients determine the type, symbolically denoted by t. Similarly but independently, r' conditions of type t' can be also imposed at $x_{O'}$. In the case of a periodic domain, the conditions at the two ends of the domain must be coupled and will be discussed separately, later.

For brevity, the set of r homogeneous conditions at x_O will be given a name codified as RrTt. If $r = 0$ or 3, only one type is possible and the type designation Tt will be omitted. If any conditions in a set are inhomogeneous, the set is inhomogeneous and given the code name RrTtX (the letter X signifies the presence of external data). The following discussion of the BCs at x_O applies equally to the similar conditions at $x_{O'}$. Examples of some useful sets of BCs are listed below:

$$\text{R0:} \quad \text{no BCs,} \qquad (3.2a)$$

$$\text{R1T0:} \quad u = 0, \qquad (3.2b)$$

$$\text{R1T1:} \quad u' = 0, \qquad (3.2c)$$

$$\text{R1T2:} \quad u'' = 0, \qquad (3.2d)$$

$$\text{R1T10}(\lambda): \quad u = \pm\lambda u', \qquad (3.2e)$$

$$\text{R2T10:} \quad u = u' = 0, \qquad (3.2f)$$

$$\text{R2T20:} \quad u = u'' = 0, \qquad (3.2g)$$

$$\text{R3:} \quad u = u' = u'' = 0, \qquad (3.2h)$$

$$\text{R3X:} \quad u = g_0, \quad u' = g_1, \quad u'' = g_2. \qquad (3.2i)$$

Of the rank-1 BCs, (3.2b)–(3.2d) are commonly discussed in textbooks (e.g., de Boor 1987). With a positive scaling constant λ, (3.2e) emulates exponential outward decay either at x_O (with "+") or at $x_{O'}$ (with "−"). Of the rank-2 BCs, (3.2g) forces u to be antisymmetric with the implicit field on the other side of the boundary, while rank-1 (3.2c) is sufficient for symmetry. The rank-3 BCs, especially the inhomogeneous R3X, will play important roles in domain nesting. Note that R0, which asserts u to be in the original class S_3, is a legitimate condition and also useful in nesting.

The general representation of $u(x) \in S_3$ that satisfies a given set of BCs can be written as the sum of two parts:

$$u(x) = \tilde{u}(x) + \hat{u}(x), \qquad (3.3)$$

where $\tilde{u}(x)$ is the general *interior* representation that satisfies the homogeneous part of the conditions and $\hat{u}(x)$ is any particular representation that satisfies the complete set of inhomogeneous conditions.

b. Homogeneous boundary conditions

For $n = 0$, 1, or 2, the rank-1 condition R1Tn at x_O requires that the nth derivative $u^{(n)}(x_O)$ to vanish. Since $\phi_m^{(n)}(x_O) = 0$ for $m \geq 2$, it follows that

$$\phi_{-1}^{(n)}(x_O)a_{-1} + \phi_0^{(n)}(x_O)a_0 + \phi_1^{(n)}(x_O)a_1 = 0, \qquad (3.4)$$

or $a_{-1} = \alpha_1 a_0 + \beta_1 a_1$, where

$$\alpha_1 = -\frac{\phi_0^{(n)}(x_O)}{\phi_{-1}^{(n)}(x_O)}, \qquad \beta_1 = -\frac{\phi_1^{(n)}(x_O)}{\phi_{-1}^{(n)}(x_O)}. \qquad (3.5)$$

The coefficients (3.5) define the required relation among the amplitudes, but they can also be used for construction of modified basis functions, $\tilde{\phi}_m$, that satisfy the given BCs by themselves. For $r = 1$, there are two of those that actually need to be modified:

$$\tilde{\phi}_0(x) = \phi_0(x) + \alpha_1\phi_{-1}(x),$$

$$\tilde{\phi}_1(x) = \phi_1(x) + \beta_1\phi_{-1}(x). \qquad (3.6)$$

The remaining ϕ_m are unmodified, but for notational consistency,

$$\tilde{\phi}_m(x) \equiv \phi_m(x) \quad \text{for } m \geq 2. \qquad (3.7)$$

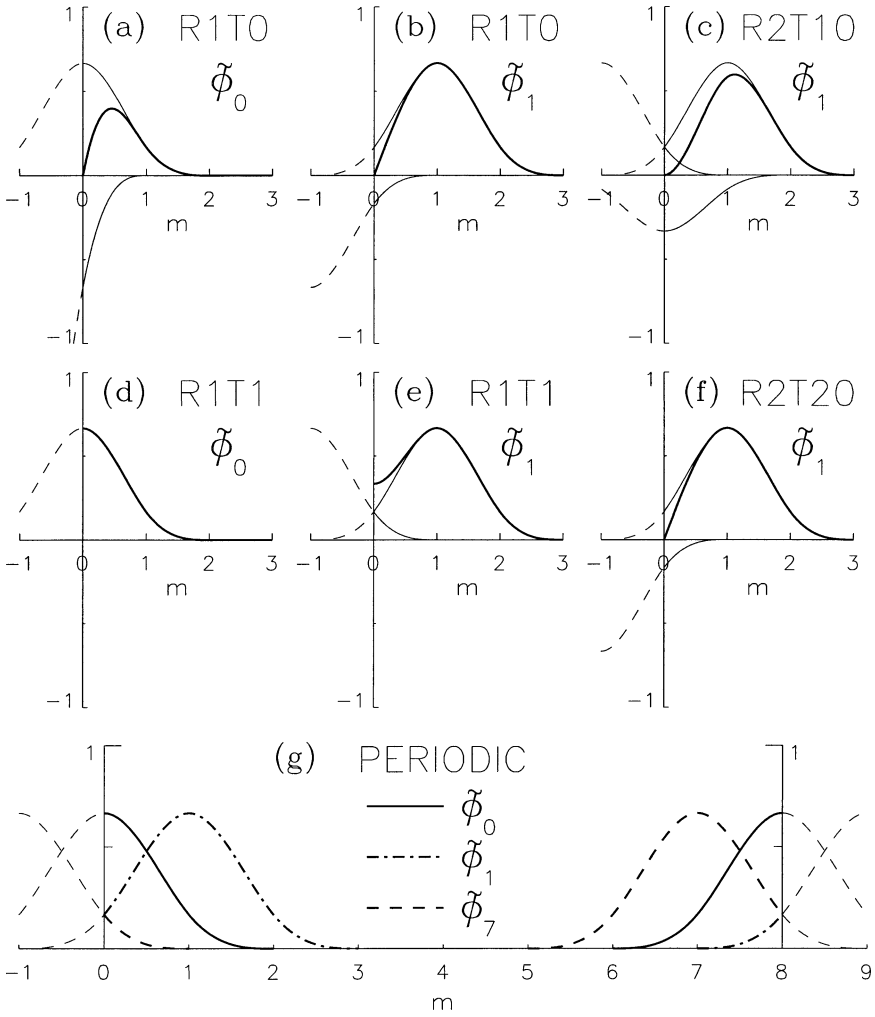

FIG. 3. Examples of the modified basis functions (thick lines) at border nodes under the boundary conditions indicated. Thin lines are constituent members of the original basis functions; thin-dashed lines are unused segments outside the domain.

Thus, for any set of amplitudes $\{\tilde{a}_0, \tilde{a}_1, \dots\}$, the general interior solution $\tilde{u}(x)$,

$r = 1$:

$$\tilde{u}(x) = \tilde{\phi}_0(x)\tilde{a}_0 + \tilde{\phi}_1(x)\tilde{a}_1 + \tilde{\phi}_2(x)\tilde{a}_2 + \cdots, \quad (3.8)$$

will automatically satisfy R1T*n*. If the rank-1 condition is imposed at $x_{O'}$, it will require $\tilde{\phi}_{\overline{m}}$ and $\tilde{\phi}_{\overline{m-1}}$ to be modified with similarly defined coefficients α_1' and β_1'. In the case of the decay condition (3.2e), these coefficients will contain the optional constant λ.

The above arguments are easily extended to the rank-2 conditions R2T*nn*′, such as (3.2f) or (3.2g). From the two simultaneous conditions at x_O, the two coefficients, α_2 and β_2, are determined by solving

$$\begin{aligned} a_2\phi_{-1}^{(n)}(x_O) + \beta_2\phi_0^{(n)}(x_O) &= -\phi_1^{(n)}(x_O), \\ a_2\phi_{-1}^{(n')}(x_O) + \beta_2\phi_0^{(n')}(x_O) &= -\phi_1^{(n')}(x_O), \end{aligned} \quad (3.9)$$

and one basis function needs to be modified,

$$\tilde{\phi}_1(x) = \phi_1(x) + \alpha_2\phi_{-1}(x) + \beta_2\phi_0(x). \quad (3.10)$$

Then, for any set of amplitudes $\{\tilde{a}_1, \tilde{a}_2, \dots\}$,

$$r = 2: \qquad \tilde{u}(x) = \tilde{\phi}_1(x)\tilde{a}_1 + \tilde{\phi}_2(x)\tilde{a}_2 + \cdots, \quad (3.11)$$

will automatically satisfy R2T*nn*′.

In the cases of R3 and R0, no basis function actually needs to be modified except for the difference in the number of participating nodes; that is,

$$r = 3: \qquad \tilde{u}(x) = \tilde{\phi}_2(x)\tilde{a}_2 + \tilde{\phi}_3(x)\tilde{a}_3 + \cdots, \quad (3.12)$$

$$r = 0: \qquad u(x) \equiv \tilde{u}(x) = \tilde{\phi}_{-1}(x)\tilde{a}_{-1} + \tilde{\phi}_0(x)\tilde{a}_0 + \cdots, \quad (3.13)$$

with $\tilde{\phi}_m \equiv \phi_m$ for every participating m.

Examples of the modified basis functions are illustrated in Fig. 3; the periodic case in the bottom panel is explained later.

c. The base-folding operator

All of the results, above, can be written in a simpler form. Let the nodal indices M be divided into mutually exclusive subsets: $\hat{M}_O$ and $\hat{M}_{O'}$ for the left and right *border* nodes, respectively, and $\tilde{M}$ for the *interior*[2] nodes:

$$\hat{M}_O = \{m | -1 \le m \le r - 2\},$$
$$\tilde{M} = \{m | r - 1 \le m \le \overline{m} - r' + 1\},$$
$$\hat{M}_{O'} = \{m | \overline{m} - r' + 2 \le m \le \overline{m} + 1\}. \quad (3.14)$$

Note that the ranks r and r' are independent, though neither can exceed 3. If r (or r') is 0, $\hat{M}_O$ (or $\hat{M}_{O'}$) is an empty set. On the other hand, $\tilde{M}$ should not be empty, requiring $\overline{m} > r + r' - 2$, or $\overline{m} > 4$ for all contingencies.

The general interior representation, which was separately obtained in (3.8) and (3.11)–(3.13), is now written in the unified form

$$\tilde{u}(x) = \tilde{\boldsymbol{\phi}}^{\mathrm{T}}\tilde{\mathbf{a}}, \quad (3.15)$$

where

$$\tilde{\boldsymbol{\phi}} = [\tilde{\phi}_m(x)]^{\mathrm{T}}_{m\in\tilde{M}}, \qquad \tilde{\mathbf{a}} = [\tilde{a}_m]^{\mathrm{T}}_{m\in\tilde{M}}. \quad (3.16)$$

The definition of the modified basis, generalized for any combination of r and r', is written as

$$\tilde{\boldsymbol{\phi}} = \boldsymbol{\Gamma}\boldsymbol{\phi}, \quad (3.17)$$

where the base-folding operator $\boldsymbol{\Gamma}$ is a rectangular matrix of $(\overline{m} + 3 - r - r')$ rows that correspond to the interior nodes $\tilde{M}$, and of $(\overline{m} + 3)$ columns for all nodes M. By dividing the columns into three sections as in (3.14), we may write $\boldsymbol{\Gamma}$ in terms of three juxtaposed submatrices,

$$\boldsymbol{\Gamma} = [\hat{\boldsymbol{\gamma}}_O, \tilde{\boldsymbol{\gamma}}, \hat{\boldsymbol{\gamma}}_{O'}], \quad (3.18)$$

where $\tilde{\boldsymbol{\gamma}}$ in the middle is a square identity matrix for the interior nodes, while $\hat{\boldsymbol{\gamma}}_O$ and $\hat{\boldsymbol{\gamma}}_{O'}$ directly depend on the rank and type of BCs at the respective boundary, as shown below:

$r, r' = 0$:

$$\hat{\boldsymbol{\gamma}}_O = [\varnothing], \qquad \hat{\boldsymbol{\gamma}}_{O'} = [\varnothing]; \quad (3.19)$$

$r, r' = 1$:

$$\hat{\boldsymbol{\gamma}}_O = \begin{bmatrix} \alpha_1 \\ \beta_1 \\ 0 \\ \vdots \\ 0 \end{bmatrix}, \qquad \hat{\boldsymbol{\gamma}}_{O'} = \begin{bmatrix} 0 \\ \vdots \\ 0 \\ \beta_1' \\ \alpha_1' \end{bmatrix}; \quad (3.20)$$

$r, r' = 2$:

[2] Depending on r and r', the interior nodes in $\tilde{M}$ do not necessarily lie inside D. In more precise terms, they are the nodes that participate in the interior representation $\tilde{u}(x)$.

TABLE 1. Folding coefficients for the homogeneous boundary conditions of rank 1 and 2.

Rank 1	α_1	β_1
R1T0	-4	-1
R1T1	0	1
R1T2	2	-1
R1T10(λ)	$\dfrac{-4}{3\lambda + 1}$	$\dfrac{3\lambda - 1}{3\lambda + 1}$

Rank 2	α_2	β_2
R2T10	1	-0.5
R2T20	-1	0

$$\hat{\boldsymbol{\gamma}}_O = \begin{bmatrix} \alpha_2 & \beta_2 \\ 0 & 0 \\ \vdots & \vdots \\ 0 & 0 \end{bmatrix}, \qquad \hat{\boldsymbol{\gamma}}_{O'} = \begin{bmatrix} 0 & 0 \\ \vdots & \vdots \\ 0 & 0 \\ \beta_2' & \alpha_2' \end{bmatrix}; \quad (3.21)$$

$r, r' = 3$:

$$\hat{\boldsymbol{\gamma}}_O = \begin{bmatrix} 0 & 0 & 0 \\ \vdots & \vdots & \vdots \\ 0 & 0 & 0 \end{bmatrix}, \qquad \hat{\boldsymbol{\gamma}}_{O'} = \begin{bmatrix} 0 & 0 & 0 \\ \vdots & \vdots & \vdots \\ 0 & 0 & 0 \end{bmatrix}. \quad (3.22)$$

The values of coefficients α_r and β_r for $r = 1$ and 2 are listed in Table 1. [A similar table in Ooyama (1987) had errors that had occurred only in preparation of the table, without affecting the results of the Global Atmospheric Research Program (GARP) Atlantic Tropical Experiment (GATE) data analysis.]

d. Inhomogeneous boundary conditions

The particular representation $\hat{u}(x)$ in (3.3) may be written in the general form

$$\hat{u}(x) = \boldsymbol{\phi}^{\mathrm{T}}\hat{\mathbf{a}}, \quad (3.23)$$

but we need only one set of amplitudes $\hat{\mathbf{a}}$ that satisfies the inhomogeneous BCs. Therefore, we assume as the rule that

$$\hat{a}_m = 0 \quad \text{for } m \in \tilde{M}, \quad (3.24)$$

and that $\hat{a}_m$ is nontrivial only at the border nodes $\hat{M}_O$ and $\hat{M}_{O'}$.

In the case of R3X at x_O, for example, three conditions

$$\phi_{-1}^{(n)}(x_O)\hat{a}_{-1} + \phi_0^{(n)}(x_O)\hat{a}_0 + \phi_1^{(n)}(x_O)\hat{a}_1 = g_n, \quad (3.25)$$

for $n = 0$, 1, and 2, will uniquely determine the amplitudes at the three border nodes. In two-dimensional problems, however, the algorithm analogous to (3.25) encounters the difficulty of over- and underdetermined nodes at the corners of a rectangular domain. In application to domain nesting, the nontrivial $\hat{a}_m$ can be determined from the coarse-node amplitudes in the adjacent domain, not by interpolation but by exact means of basis conversion; such a procedure is extendable to multidimensions without the corner problem.

e. The periodicity condition

Although the present cubic-spline method is primarily designed for the nonperiodic finite domain, it can also be applied to a periodic domain D, where the outer bounds x_O and $x_{O'}$ are not true boundaries but merely indicators of the basic cycle in a cyclically continuous space. Nevertheless, we can continue to use the formalism for the homogeneous BCs, by coupling the border nodes at both ends as to emulate the functionality of the interior nodes. The number of the resulting ''interior'' nodes should be $\overline{m}$, but their exact location may be anywhere within M.

For the sake of definiteness, we choose

$$\begin{aligned} \hat{M}_O &= \{-1\}, \\ \tilde{M} &= \{0, 1, 2, \ldots, \overline{m} - 1\}, \\ \hat{M}_{O'} &= \{\overline{m}, \overline{m} + 1\}, \end{aligned} \tag{3.26}$$

and modify the basis functions in $\tilde{M}$ by wrapping around with those in $\hat{M}_O$ or $\hat{M}_{O'}$ (see Fig. 3g for $\overline{m} = 8$), so that

$$\tilde{\phi}_0(x) = \phi_0(x) + \phi_{\overline{m}}(x),$$

$$\tilde{\phi}_1(x) = \phi_1(x) + \phi_{\overline{m}+1}(x),$$

$$\tilde{\phi}_{\overline{m}-1}(x) = \phi_{\overline{m}-1}(x) + \phi_{-1}(x), \quad \text{and} \tag{3.27}$$

$$\tilde{\phi}_m(x) = \phi_m(x) \quad \text{for } 2 \le m \le \overline{m} - 2. \tag{3.28}$$

With these definitions, the general form of periodic $\tilde{u}(x)$ is identical to (3.15), except for the following substitution in the composite definition (3.18) of $\mathbf{\Gamma}$:

$$r = 1, \qquad r' = 2:$$

$$\hat{\boldsymbol{\gamma}}_O = \begin{bmatrix} 0 \\ 0 \\ \vdots \\ 0 \\ 1 \end{bmatrix}, \qquad \hat{\boldsymbol{\gamma}}_{O'} = \begin{bmatrix} 1 & 0 \\ 0 & 1 \\ 0 & 0 \\ \vdots & \vdots \\ 0 & 0 \end{bmatrix}. \tag{3.29}$$

4. Cubic-spline transforms

a. Representation of field variables

Any function $\breve{u}(x)$ defined in D may be approximated by a cubic-spline function $u(x)$ from S_3 by the method of least squares. For reasons that will be discussed in section 5, an optional constraint on the third-order derivative is also included in the fitting procedure. Thus, the present task is to minimize the integral J,

$$J = \int_D \{[\breve{u}(x) - u(x)]^2 + \epsilon_q(x)[u'''(x)]^2\}\, dx, \tag{4.1}$$

by varying the nodal amplitudes that define $u(x)$. The non-negative weight function $\epsilon_q(x)$ in the constraint term is selectable for achieving desired effects but is usually a constant in simple applications.

In the case of no boundary condition, R0, every a_m in (2.7) is a free variational parameter, and the minimization of J leads to the matrix equation for $\mathbf{a}$,

$$(\mathbf{P} + \mathbf{Q})\mathbf{a} = \mathbf{b}, \tag{4.2}$$

where, for $m, m' \in M$,

$$\mathbf{b} = [b_m]^{\mathrm{T}}, \qquad b_m = \int_D \phi_m(x)\breve{u}(x)\, dx, \tag{4.3a}$$

$$\mathbf{P} = [p_{mm'}], \qquad p_{mm'} = \int_D \phi_m(x)\phi_{m'}(x)\, dx, \tag{4.3b}$$

$$\mathbf{Q} = [q_{mm'}], \qquad q_{mm'} = \int_D \epsilon_q(x)\phi'''_m(x)\phi'''_{m'}(x)\, dx. \tag{4.3c}$$

If boundary conditions are imposed, the general form of $u(x)$ is the sum of (3.15) and (3.23):

$$u(x) = \tilde{\boldsymbol{\phi}}^{\mathrm{T}}\tilde{\mathbf{a}} + \hat{\boldsymbol{\phi}}^{\mathrm{T}}\hat{\mathbf{a}}, \tag{4.4}$$

although $\hat{\mathbf{a}} \equiv 0$ in the case of homogeneous BCs or periodicity. Since only the $\tilde{a}_m$ for $m \in \tilde{M}$ are free variational parameters, the minimization of J leads to the matrix equation for $\tilde{\mathbf{a}}$,

$$(\tilde{\mathbf{P}} + \tilde{\mathbf{Q}})\tilde{\mathbf{a}} = \tilde{\mathbf{b}}, \tag{4.5}$$

where

$$\tilde{\mathbf{b}} = \mathbf{\Gamma}[\mathbf{b} - (\mathbf{P} + \mathbf{Q})\hat{\mathbf{a}}], \tag{4.6a}$$

$$\tilde{\mathbf{P}} = \mathbf{\Gamma}\mathbf{P}\mathbf{\Gamma}^{\mathrm{T}}, \qquad \tilde{\mathbf{Q}} = \mathbf{\Gamma}\mathbf{Q}\mathbf{\Gamma}^{\mathrm{T}}. \tag{4.6b}$$

Since all the information specifying the particular BCs is contained in the few nontrivial elements of $\hat{\mathbf{a}}$ and $\mathbf{\Gamma}$, the conversion of (4.3) to (4.6) requires little calculation. It is also noted that, after solving (4.5) for $\tilde{\mathbf{a}}$, (4.4) may be rewritten in terms of the unmodified basis as

$$\mathbf{a} = \mathbf{\Gamma}^{\mathrm{T}}\tilde{\mathbf{a}} + \hat{\mathbf{a}}, \tag{4.7a}$$

$$u(x) = \boldsymbol{\phi}^{\mathrm{T}}\mathbf{a}. \tag{4.7b}$$

This is different from (2.7) in that a is now reconstructed to satisfy the BCs. We shall call (4.7) the *open* form of the representation because the amplitudes are opened up to all nodes; in contrast, (4.4) will be called the *closed* form.

For convenience of later reference, the process of calculating (4.3a) is called the SB transform,

$$\mathbf{b} = \mathrm{SB}[\breve{u}]; \tag{4.8}$$

the process of calculating (4.7a) through (4.6a) and (4.5) the SA transform,

$$\mathbf{a} = \mathrm{SA}[\mathbf{b}]; \tag{4.9}$$

and (4.7b) the SI transform,

$$u(x) = \mathrm{SI}[\mathbf{a}], \tag{4.10}$$

which is extendable to the derivatives of $u(x)$, by the similar transform, SI_x or SI_{xx},

$$u'(x) = SI_x[\mathbf{a}] = (\boldsymbol{\phi}')^T\mathbf{a},$$
$$u''(x) = SI_{xx}[\mathbf{a}] = (\boldsymbol{\phi}'')^T\mathbf{a}. \quad (4.11)$$

In the above grouping of processes, the implementation of the BC is concentrated in the SA transform. The special case of SA, in which no derivative constraint ($\epsilon_q \equiv 0$) is applied, will be denoted as SA_0. If $\breve{u}(x)$ is already a cubic-spline function satisfying the BCs, the ordered product of SI, SA_0, and SB, and its cyclic permutations, are the identity operators,

$$u = SI[SA_0[SB[u]]],$$
$$\mathbf{b} = SB[SI[SA_0[\mathbf{b}]]],$$
$$\mathbf{a} = SA_0[SB[SI[\mathbf{a}]]]. \quad (4.12)$$

These relationships should be preserved, as discussed below, when the integrals in (4.3) are replaced by discrete sums.

b. Discrete quadrature

In general applications, the given function $\breve{u}(x)$ is known only at a finite number, $\bar{\imath}$, of discrete points, x_i, in D, and the integral in (4.3a) for each $m \in M$ will be estimated by summation:

$$b_m = \sum_{i=1}^{\bar{\imath}} \phi_m(x_i)\breve{u}(x_i)w_i, \quad (4.13)$$

where the w_i are appropriate weights. In the case of analyzing observational data (e.g., Ooyama 1987), the sampling points are part of the given dataset. In the CST method for a numerical model, x_i are the quadrature points where $\breve{u}(x_i)$ is evaluated from the model equations, and may be chosen to suit the purpose.

In order to maintain uniformity of representation, every nodal cell in D will be handled by the same quadrature scheme. Let m_c be the index of a cell bounded by two nodes, (x_{m_c}, x_{m_c+1}), and M_c the set of all possible m_c:

$$M_c = \{m_c \mid 0 \le m_c \le \bar{m} - 1\}. \quad (4.14)$$

The integration over each cell m_c is performed by the $\bar{\mu}$th degree Gaussian quadrature scheme, for which the quadrature points δ_μ (relative to x_{m_c}) and the weight factors w_μ (independent of m_c), for $\mu = 1, 2, \ldots, \bar{\mu}$, are preset. Thus, the sequential index i and the quadrature points x_i can be given in terms of the two indices (μ, m_c), that is,

$$i = \mu + \bar{\mu}m_c,$$
$$x_i \equiv x_{\mu,m_c} = \delta_\mu + x_{m_c}. \quad (4.15)$$

The values of x_i and $w_i \equiv w_\mu$, both normalized for $\Delta x = 1$, are shown in Fig. 4. Note that the standard numerical values, such as found in Davis and Polonsky (1964), are defined for the interval $(-1, 1)$, and our values have been adapted to the interval (0, 1).

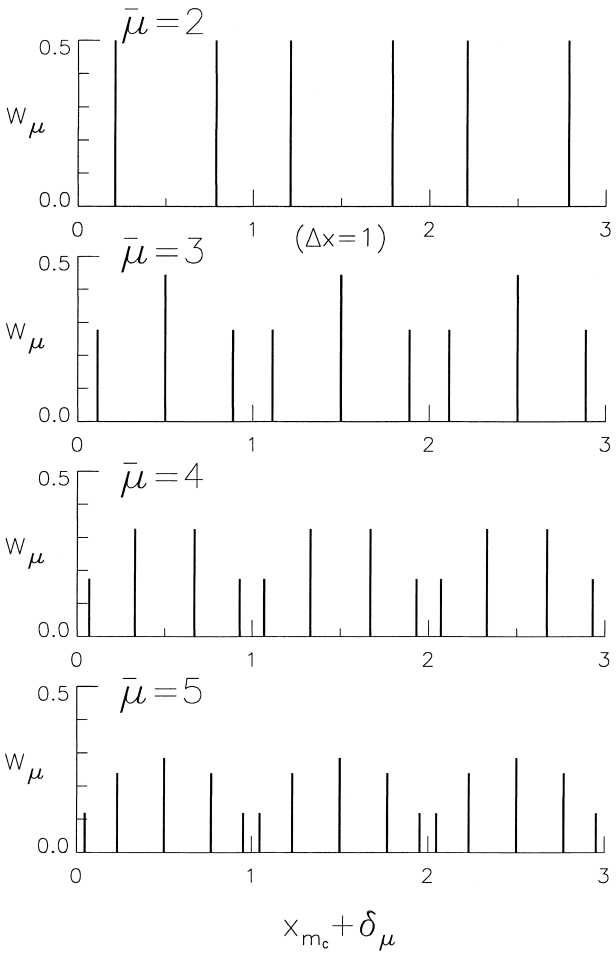

FIG. 4. The sampling points (abscissa) and weights (ordinate) of the $\bar{\mu}$th-degree Gaussian quadrature: (a)–(d) for $\bar{\mu} = 2$, 3, 4, and 5, respectively. The values are for the normalized interval $\Delta x = 1$.

Now, (4.13) is formally written as

$$b_m = \sum_{m_c \in M_c} \left[\sum_{\mu=1}^{\bar{\mu}} \phi_m(x_{\mu,m_c})\breve{u}(x_{\mu,m_c})w_\mu \right]. \quad (4.16)$$

However, ϕ_m identically vanishes at x_{μ,m_c} for $m_c < m - 2$ or $m_c > m + 1$; thus, the summation over m_c is actually limited to four cells in the neighborhood of the node x_m, or to fewer cells if the node is near the boundary. Thus, the amount of calculation for the SB transform, that is, b_m for every $m \in M$, increases only linearly with $\bar{\mu}\bar{m}$. The greater $\bar{\mu}$ is, the smaller the risk of aliasing (see the appendix), but the physical calculation of $\breve{u}$, the payload of the model (section 6), also increases with $\bar{\mu}$. In most applications, $\bar{\mu} = 2$ or, at most, 3 has been found acceptable.

It may be noted that, in the Fourier spectral model,

the amount of corresponding calculation by FFT[3] is the order of $(\overline{\mu}\,\overline{m})\ln(\overline{\mu}\,\overline{m})$ and that, if the spline basis were orthogonalized as mentioned in section 2b, the calculation would have been the order of $\overline{\mu}\,\overline{m}^2$.

If the integrand is a polynomial of nth degree, the $\overline{\mu}$th degree Gaussian quadrature yields the exact integral provided that $n < 2\overline{\mu}$. Since the integrand in (4.3b) is a sixth-degree polynomial in each cell, the estimate by the Gaussian scheme,

$$p_{mm'} = \sum_{m_c \in M_c} \left[\sum_{\mu=1}^{\overline{\mu}} \phi_m(x_{\mu,m_c}) \phi_{m'}(x_{\mu,m_c}) w_\mu \right], \quad (4.17)$$

will be exact if $\overline{\mu} \geq 4$. However, since $\breve{u}(x)$ is not necessarily a polynomial of any degree, it is wasteful to employ an unnecessarily high value of $\overline{\mu}$ in the SB transform, which needs to be repeatedly performed in the course of model time integration. More importantly, the discretized transforms must uphold the identity relations (4.12), in order to avoid slow drifts of model variables in places where nothing is physically happening. For this goal, it is necessary and sufficient to employ the same $\overline{\mu}$ in both (4.16) and (4.17); unnecessary accuracy in (4.17) alone is actually harmful.

The nonzero cells of ϕ_m and $\phi_{m'}$ intersect only when $|m - m'| \leq 3$, and the summation over m_c is again limited to those few intersecting cells. Consequently, **P** is a seven-diagonal banded matrix and, if $\overline{\mu} \geq 2$, it is positive definite. When $\overline{\mu} = 1$, the sampling point is at the midpoint of the cell, and **P** becomes a singular matrix. Other quadrature schemes, such as the trapezoidal, can produce a positive-definite **P** even with only one sampling point per cell, if the point is at the node itself. However, any computational advantage of such a low-density sampling will be offset by the risk of unmitigated aliasing in the SB transform.

Since the weight factor $\epsilon_q(x)$ is a constant or smooth function in D, a scheme similar to (4.17) may be used for the estimate of the integral in (4.3c),

$$q_{mm'} = \sum_{m_c \in M_c} \left[\sum_{\mu=1}^{\overline{\mu}} \epsilon_q(x_{\mu,m_c}) \phi'''_m(x_{\mu,m_c}) \phi'''_{m'}(x_{\mu,m_c}) w_\mu \right], \quad (4.18)$$

which, like (4.17), vanishes unless $|m - m'| \leq 3$. Thus, **Q** is also a seven-diagonal banded matrix and should be non-negative definite.

The SI transform is the inverse transform of the spline amplitudes to the field values at any given set of points in D. If those values are required for tabulation purposes, for example, the output can be made at equally spaced points without the use of an extraneous interpolation scheme. In order to uphold the identity relations (4.12), however, $u(x)$ must be available at the quadrature points (4.15) of the SB transform. Therefore, the SI transform normally implies

$$u(x_i) \equiv u(x_{\mu,m_c}) = \sum_{m \in M} \phi_m(x_{\mu,m_c}) a_m, \quad (4.19)$$

in which the summation over m is again limited to a few neighbors of m_c, so that the computational cost of the SI transform is again the order of $\overline{\mu}\,\overline{m}$; the derivatives of u at x_i are similarly obtained by replacing ϕ_m by its derivatives. Note that the BC for u is already incorporated in a_m of the open form (4.7). The set of x_i is called the quadrature micromesh or, informally, the *mish*, and the physical equations (PEs in section 6) are evaluated on the sequential mish. (Only the transforms are calculated by double-indexing.) The unequal spacing of x_i chosen for the Gaussian quadrature has no adverse effect, since we do not employ spatial finite differences.

c. Algorithm for the SA transform

As was discussed above, both **P** and **Q** are symmetric, seven-diagonal banded matrices of the same structure, and **P** + **Q** is positive definite. The border-folded matrix, $\tilde{\mathbf{P}} + \tilde{\mathbf{Q}}$, retains the same characteristics, except for a few extra corner elements in the periodic case, and can be triangularized by Gaussian elimination. The standard LDL^T method (e.g., Golub and Van Loan 1996) preserves the bandedness, and the amount of calculation is of the order of $\overline{m}$, although the corner elements add a few more steps in the case of periodicity.

In 2D (and 3D) applications, $\tilde{\mathbf{P}} + \tilde{\mathbf{Q}}$ becomes a doubly banded matrix, that is, a banded supermatrix whose elements themselves are banded matrices. The outer bandedness can be easily exploited, but it is a challenge to preserve also the inner bandedness, although we have an algorithm that partially utilizes the inner bandedness. (Details are omitted in deference to a reviewer.)

d. Other useful transforms

In modeling physical equations, it may occur that a function $\breve{f}(x)$ (e.g., an eddy flux) is numerically calculated in D, but that the SB transform of its derivative (the flux divergence) is desired:

$$\mathbf{b} = \mathrm{SB}[\breve{f}']. \quad (4.20)$$

It can be calculated directly from $\breve{f}(x)$, without differentiation, by

$$\mathbf{b} = [\boldsymbol{\phi}\breve{f}]_{x_O}^{x_{O'}} - \mathrm{SB}_x[\breve{f}], \quad (4.21)$$

where

$$\mathrm{SB}_x[\breve{f}] \equiv \int_D \boldsymbol{\phi}'\breve{f}\, dx, \quad (4.22)$$

and the boundary values of $\breve{f}$ at x_O and $x_{O'}$ are usually known or assumable.

On other occasions (e.g., the diagnostic calculation of hydrostatic pressure), it may be necessary to integrate a numerically given function $\breve{v}(x)$. Let $u(x)$ of (2.7) be

[3] In FFT, the $\overline{\mu}\,\overline{m}$ sampling points should be equally spaced. In nonlinear models, $\overline{\mu} = 2$ or 3 is also recommended to minimize aliasing.

the cubic-spline representation of the indefinite integral, and $v(x)$ the derivative of $u(x)$:

$$u(x) \simeq \int^x \check{v}\, dx + C, \qquad v(x) = u' = (\boldsymbol{\phi}')^{\mathrm{T}}\mathbf{a}. \tag{4.23}$$

Then, except for the constant of integration C, the problem becomes that of finding $\mathbf{a}$ by fitting $v(x)$ to $\check{v}(x)$, which leads to the matrix equation

$$\mathbf{P}^{(1)}\mathbf{a} = \mathrm{SB}_x[\check{v}], \tag{4.24}$$

where

$$\mathbf{P}^{(1)} \equiv \int_D \boldsymbol{\phi}'(\boldsymbol{\phi}')^{\mathrm{T}}\, dx. \tag{4.25}$$

Once $\mathbf{a}$ is determined from (4.24), the constant C can easily be fixed by a boundary condition to the integral.

5. The derivative constraint as a low-pass filter

Although the representation in S_3 is continuous, it has certain microscopic errors (see the appendix) due to the use of discrete nodes. As in a finite Fourier series, only the cosine wave has a representation at the Nyquist wavelength, $2\Delta x$. Unlike the Fourier, however, the disparity between cosine and sine lingers on up to about 3 or $4\Delta x$ waves. Thus, even in static applications, these short waves demonstrate the graininess of representation. In dynamic applications, nonlinear processes may continually generate smaller-scale components, and, if they are allowed to accumulate near the Nyquist scale, the representation error can lead to numerical instability. As a means of abating these problems, a third-order derivative constraint (DC) was incorporated in (4.1).

The fact that the constraint acts as a low-pass filter can be easily demonstrated if $u(x)$ is not a spline function but is an analytic function, so that the minimization of (4.1) can be written as the variational problem,

$$\delta J = 2\int_D [(u - \check{u})\delta u + \epsilon_q u'''(\delta u)'''] \, dx = 0, \tag{5.1}$$

in which ϵ_q is assumed to be a constant. For $\check{u} = \exp(ikx)$ in a periodic domain, the Euler–Lagrange equation,

$$u - \check{u} = \epsilon_q(\partial_x)^6 u, \tag{5.2}$$

has the solution

$$u = R\exp(ikx) \quad \text{with} \quad R = (1 + \epsilon_q k^6)^{-1}. \tag{5.3}$$

If both the wavenumber k and the weight factor ϵ_q are expressed in terms of the nondimensional wavelength l (in units of Δx) and a constant value l_q,

$$k = \frac{2\pi}{l\Delta x}, \qquad \epsilon_q = \left(\frac{l_q\Delta x}{2\pi}\right)^6, \tag{5.4}$$

the spectral response function R is written as

$$R(l, l_q) = [1 + (l_q/l)^6]^{-1}. \tag{5.5}$$

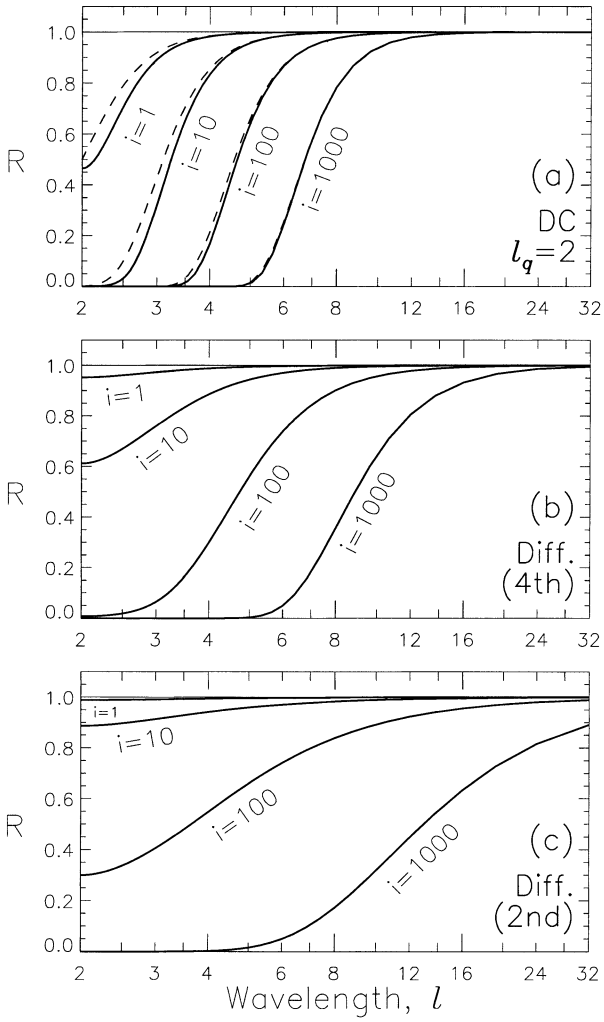

FIG. 5. The spectral response function R for (a) the DC with l_q = 2 (analytic approximation by dashed lines), (b) fourth-order diffusion with K^* = 0.003, and (c) second-order diffusion with K^* = 0.003. In each panel, the iteration counts for repeated applications are indicated as i = 1, 10, 100, and 1000. The abscissa l is the normalized wavelength in units of Δx.

The response function of the actual DC filter by the cubic-spline transform is obtained only numerically, and the result is shown in Fig. 5a by a solid line (i = 1) together with its analytic approximation (5.5) by a dashed line, both for l_q = 2. The two curves asymptotically merge into each other for large l, while there are slight differences at small $l \lesssim 4$. Thus, the interpretation of l_q as the half-response point in (5.5) does not strictly apply to the correct response, but we shall continue to express ϵ_q in terms of l_q as defined in (5.4). If ϵ_q is a function of x, so also is l_q.

Since the filter is applied every time the SA transform is performed, its long-term effect on the time integration of a model needs to be considered. Thus, Fig. 5a also depicts the cumulative effects of the filter when it is successively applied 10, 100, and 1000 times. If the

model physics does not generate new disturbances, the figure implies, by extension, that all spatial variation would eventually be filtered out. However, the significance of the sixth-order taper in (5.5) may be appreciated more realistically by comparison with other filtering methods.

In atmospheric models, the most common method for this purpose is to include diffusion in the prognostic equations, in terms of either second-order or fourth-order derivatives,

$$\partial_t u = K_{2\text{nd}}\partial_x^2 u, \qquad \partial_t u = K_{4\text{th}}\partial_x^4 u, \tag{5.6}$$

where the coefficients of diffusivity may be expressed in terms of the nondimensional coefficient K^* as

$$K_{2\text{nd}} = K^*(\Delta x)^2(\Delta t)^{-1},$$
$$K_{4\text{th}} = K^*(\Delta x)^4(\Delta t)^{-1}. \tag{5.7}$$

Applying the finite-difference approximations to the derivatives, the spectral response functions are obtained as

$$R_{2\text{nd}}(l, K^*) = 1 - 4K^* \sin^2(\pi/l) \sim 1 - K^*(2\pi/l)^2,$$
$$R_{4\text{th}}(l, K^*) = 1 - 16K^* \sin^4(\pi/l) \sim 1 - K^*(2\pi/l)^4. \tag{5.8}$$

The lines ($i = 1$) in Figs. 5b,c depict $R_{4\text{th}}$ and $R_{2\text{nd}}$, respectively, both for $K^* = 0.003$. The net effects of repeated applications are also shown.

The particular value of K^*, above, is the one that has been suggested by Grell et al. (1995) for use in the fifth-generation Pennsylvania State University–National Center for Atmospheric Research (Penn State–NCAR) Mesoscale Model (MM5) as the *background* horizontal diffusion. If the model physics are highly nonlinear, the background diffusion as shown may not be sufficient to cope with rapidly accumulating numerical errors near the Nyquist scale, so that MM5, as well as many other similar models, requires nonlinear parameterization of K^* for enhanced diffusion. As for the DC filter, the value of l_q to choose is also somewhat dependent on the physical equations, although $l_q = 2$ was large enough to avoid computational instability in all the nonlinear examples demonstrated in Ooyama (2001), while $l_q = 1.8$ (though not 1.5) was successful in certain cases.

As to the cumulative effects of repeated filter applications, the MM5 background diffusion alone causes far greater dissipation of large scales than does the DC filter with $l_q = 2$. It is of course possible to introduce sixth- or higher-order diffusion in gridpoint models, though the finite-difference schemes may have to be modified near the boundary of a finite domain, while the DC filter in the integral transform applies uniformly over the domain up to the boundary. As was demonstrated in Ooyama (2001), the sixth-order tapered DC filter does not interfere with second-order diffusion, if the latter is part of the modeled physics. (Also see examples in sections 7 and 8.)

6. The general schedule of time integration

The primary application of the CST method is to the time integration of nonlinear meteorological equations, which may be expressed in the Eulerian form as a Cauchy problem:

$$\partial_t u = \text{PE}(u, u', u''), \tag{6.1}$$

where $u \equiv u(x, t)$ symbolically stands for all the prognostic variables of a physical system and PE the equal number of differential expressions defining the system. Since the spatial domain is finite in usual applications, each variable requires an appropriate set of boundary conditions. Dissipative mechanisms can be included in PE for their physical effects; as discussed in the preceding section, they are not required for computational reasons. Note that calculation of PE, including a necessary number of diagnostic equations, is the payload of the model.

The time dependence of u in (6.1) is discretized in finite steps of Δt, and the flow diagrams of the time-stepping procedures are shown in Fig. 6a for the leapfrog (LF) scheme and Fig. 6b the second-order Adams–Bashforth (AB) scheme. In either case, the scheme basically follows the spectral transform method (Orszag 1970; Machenhauer 1979), so that the variables are shuttled by cubic-spline transforms between the cubic-spline amplitudes and physical space, rather than applying the Galerkin method directly to the usually nonlinear and nonself-adjoint PEs.

The PEs can be written in either the conservative flux form or the advective form. The latter is presumed in Fig. 6, and the SI_x transform generates individual derivatives as input to PEs; if necessary, the second derivatives may also be obtained by SI_{xx}. If the flux form is employed, the differentiation of fluxes F should be made by the SB_x transform after PEs. Since u is differentiable, the two forms produce exactly the same result.

In global spectral models on the spherical harmonic basis, it is common to express the velocity in terms of the streamfunction and velocity potential, and the computational advantage of Laplacian operator is preferred to more expensive transforms for individual partial derivatives. In the present method, even in multidimensional applications, the velocity will be expressed in terms of vector components, so that there will be no need for extraneous boundary conditions for those scalar variables in finite-domain applications. Besides, the SI transforms are relatively inexpensive.

The output from PEs is the time tendency of u, which is divided into several categories depending on their destinations. In Fig. 6, $\dot{u}$ signifies the fully calculated tendency terms that need straightforward conversion by SB, while F denotes the calculated fluxes that are yet to be differentiated by SB_x. For computational stability, certain tendency terms due to eddy diffusion, Rayleigh damping, etc., need to be time delayed and are combined

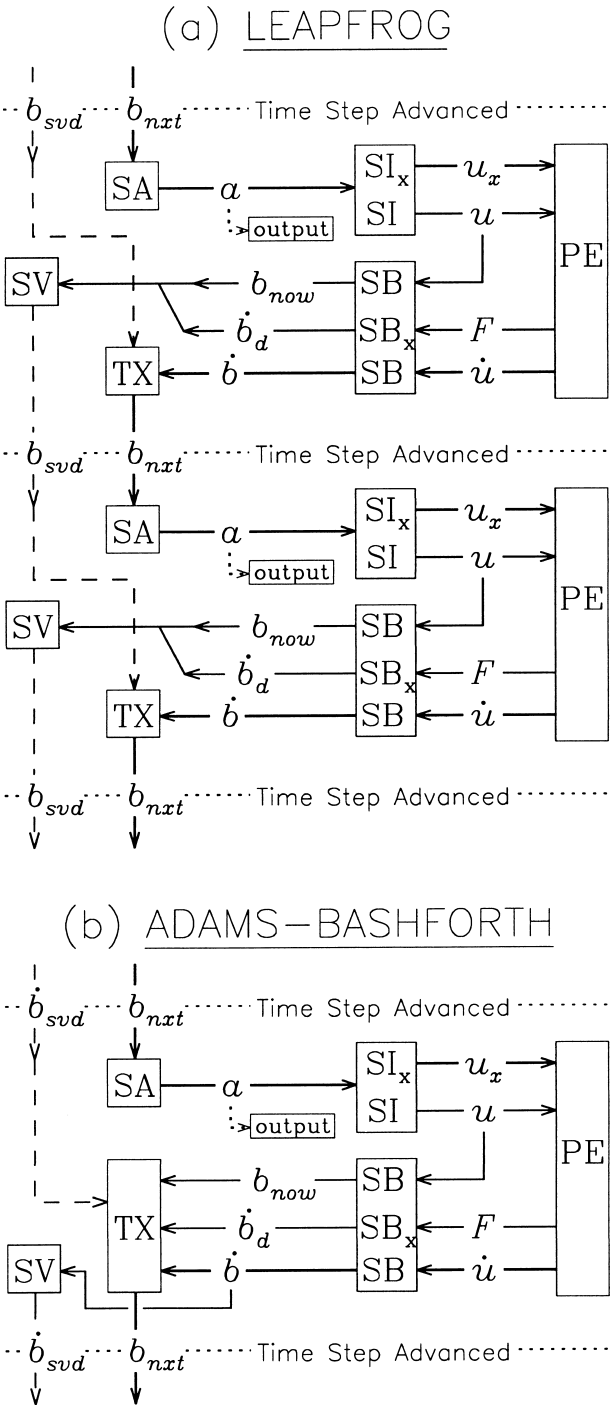

FIG. 6. Time integration schedules: (a) leapfrog scheme, and (b) Adams–Bashforth scheme.

in $\dot{\mathbf{b}}_d$, while the rest that immediately participate in the time extrapolation TX are represented by $\dot{\mathbf{b}}$. In addition, the current u is converted by SB to $\mathbf{b}_{\text{now}}$, which, due to the DC filter in SA, is not the same as $\mathbf{b}_{\text{nxt}}$ from the previous time step. Note that the chronological records of a model run are output at designated time steps in the open form of nodal amplitudes **a**, from which all the physical variables and their derivatives are recoverable in postanalysis at any spatial point.

The input to the next time step is carried in two forms of **b**, which are generated by the scheme-dependent procedures, TX and SV. For the LF scheme of Fig. 6a,

$$\text{TX:} \qquad \mathbf{b}_{\text{nxt}} \Leftarrow \mathbf{b}_{\text{svd}} + 2\Delta t\dot{\mathbf{b}}, \tag{6.2}$$

$$\text{SV:} \qquad \mathbf{b}_{\text{svd}} \Leftarrow \mathbf{b}_{\text{now}} + 2\Delta t\dot{\mathbf{b}}_d, \tag{6.3}$$

where $\mathbf{b}_{\text{svd}}$ in (6.2) is the one saved in the preceding time step and is being redefined in (6.3) as the currently saved. One notorious problem of the LF scheme is its indifference to $2\Delta t$ oscillations (the undamped computational mode), which may be forced by a forward initial step or many other causes. This mode can be damped by an Asselin (1972) filter, which is implemented by replacing (6.3) with

$$\text{SV:} \qquad \mathbf{b}_{\text{svd}} \Leftarrow (1 - \nu_{\text{ass}})(\mathbf{b}_{\text{now}} + 2\Delta t\dot{\mathbf{b}}_d) + \frac{\nu_{\text{ass}}}{2}(\mathbf{b}_{\text{nxt}} + \mathbf{b}_{\text{svd}}), \tag{6.3a}$$

where the input $\mathbf{b}_{\text{svd}}$ is the one from the preceding step, but $\mathbf{b}_{\text{nxt}}$ is the current one calculated by (6.2), and ν_{ass} is Asselin's coefficient.

Although the so-called lattice separation is often associated with instability of the LF scheme in gridpoint models, the space–time coupling on Nyquist scales does not occur with our method, and the Asselin filter can be omitted in many applications. However, as was mentioned in Ooyama (2001), in marginally saturated areas of a moist model, the phase change of water substance could become adversely coupled with the timewise oscillation due to the leapfrog scheme. An Asselin filter with $\nu_{\text{ass}} = 0.1$ was sufficient to maintain numerical stability.

In the AB scheme of Fig. 6b, for which

$$\text{TX:} \qquad \mathbf{b}_{\text{nxt}} \Leftarrow \mathbf{b}_{\text{now}} + \frac{\Delta t}{2}(3\dot{\mathbf{b}} - \dot{\mathbf{b}}_{\text{svd}}) + \Delta t\dot{\mathbf{b}}_d, \tag{6.4}$$

$$\text{SV:} \qquad \dot{\mathbf{b}}_{\text{svd}} \Leftarrow \dot{\mathbf{b}}, \tag{6.5}$$

the computational mode in time is naturally damped. On the other hand, the primary mode is known to be weakly but unconditionally unstable for certain short waves unless some damping mechanisms are postulated in the system. In our applications, the DC filter in the SA transform apparently takes care of the need, and the AB scheme is stable without dissipative terms in PEs, as long as Δt is within a limit (see below).

In the AB scheme, the history-carrying information in $\mathbf{b}_{\text{now}}$ is filtered by SA every time step, while, in the LF scheme, it occurs every other time step, although the small-scale, time-sensitive components in $\dot{\mathbf{b}}$ are filtered every step in both schemes. This fact should be remembered when the need arises to scrutinize model results. However, due to the sharp taper in the filter

response, differences between the two schemes are very subtle. In our comparison tests involving the successive generation of convective cells in a squall line (Ooyama 2001), we did not find clear evidence that AB is superior to LF, or vice versa.

If c represents the maximum wave speed that is possible in the physical system, both the LF and AB schemes require for stability that the Courant number be limited by

$$c\Delta t(\Delta x)^{-1} \lesssim 0.4. \tag{6.6}$$

This limit is slightly greater than the analytic limit π^{-1}, due to the fact that the spline representation is not quite analytic. However, it is prudent to consider π^{-1} to be the practical limit, since computational dispersion rapidly increases with the ratio above 0.3 as shown in section 7.

When the modeled system is a nonhydrostatic compressible atmosphere, acoustic waves are a possible mode of solution and the speed of sound will severely restrict the size of stable Δt, even though acoustic waves carry very little information of meteorological significance. There are many proposals to cope with this acoustic problem but, as was discussed in Ooyama (2001), we adopt Burridge's (1975) two-step formulation of the semi-implicit method. In the first step, all the prognostic variables are explicitly predicted by the LF (or AB) scheme for Δt that is small enough only for gravity waves and other meteorological modes of solution. The explicit results, then, are implicitly adjusted in the second step, which effectively slows down the acoustic waves so that they are not a factor in determining stability. This acoustic adjustment (AA) procedure can be formulated in terms of the cubic-spline amplitudes. Thus, the flow diagrams of Fig. 6 will remain exactly the same, except that the AA procedure is inserted immediately after the SA transform.

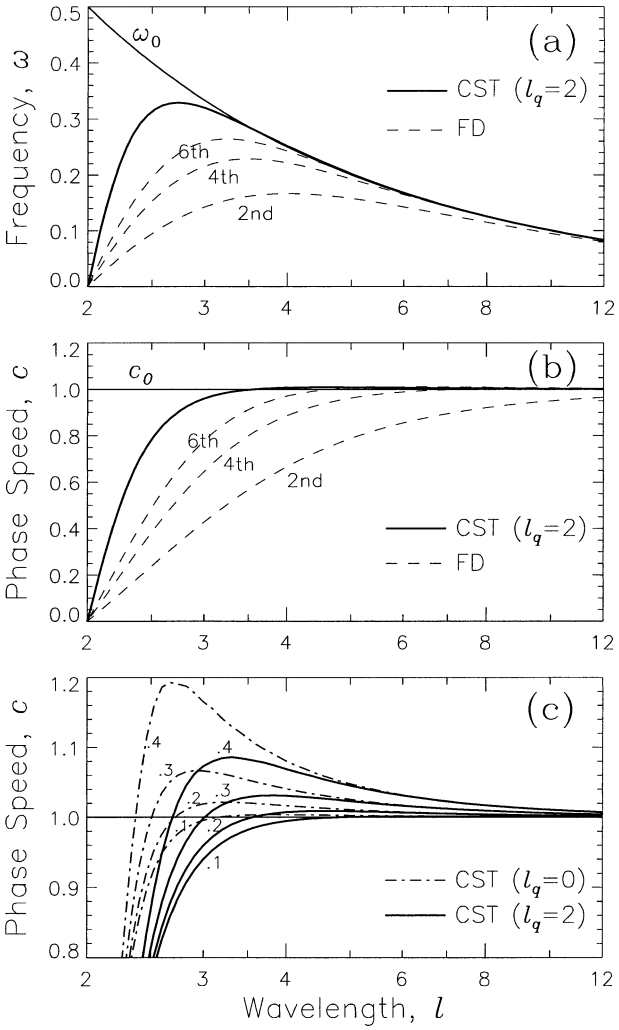

FIG. 7. Comparison, in linear advection, of the CST method (solid lines) with the finite-difference methods of various orders (FD, dashed lines), in terms of (a) the frequency, and (b) the phase speed; the Courant number is half the critical value of each method. The abscissa is the normalized wavelength. Also shown in (c) is an enlarged view of the phase speeds by the CST method, with the DC filter (solid) and without (dotted–dashed); the Courant number is varied between 0.1 and 0.4.

7. Linear advection

a. Dispersion relations

The simplest numerical problem that is relevant to meteorological applications is the advection of disturbances. We shall first consider the linearized equation for a dependent variable u,

$$\partial_t u + c_0 \partial_x u = 0, \tag{7.1}$$

with a constant advection speed c_0 in a 1D periodic domain of x. For the initial condition $u(x) = \exp(i2\pi kx)$ at $t = 0$, the solutions by various numerical methods may be in the general form

$$u(x, t) = A(t)e^{i2\pi(kx-\omega t)}, \tag{7.2}$$

where k is the wavenumber, ω the frequency, and A the amplitude. Also definable are the wavelength $l = 1/k$, the phase speed $c = \omega/k$, and the group velocity $c_g = d\omega/dk$. For the analytic (exact) solution of (7.1), it holds that $\omega = \omega_0 = c_0/k$, $c = c_g = c_0$, and $A = 1$.

The comparison of the numerical solutions by the CST method, with $l_q = 2$, and the second-, fourth-, and sixth-order finite-difference (FD) methods, without diffusion, are presented in Figs. 7a and 7b in terms of the frequency and phase speed, respectively. The time discretization is the second-order centered difference (LF) in all cases. The illustrations assume $c_0 = 1$ and $\Delta x = 1$, so that the wavelength l on the abscissa is in units of Δx. The Courant number, which is now numerically equivalent to Δt, is taken to be a half of the respective stability limit in each case. Namely, $\Delta t = 0.5$, 0.36, and 0.32, in the increasing orders of FD, and $\Delta t = 0.2$ for CST.

The phase speeds in CST are more accurate at shorter

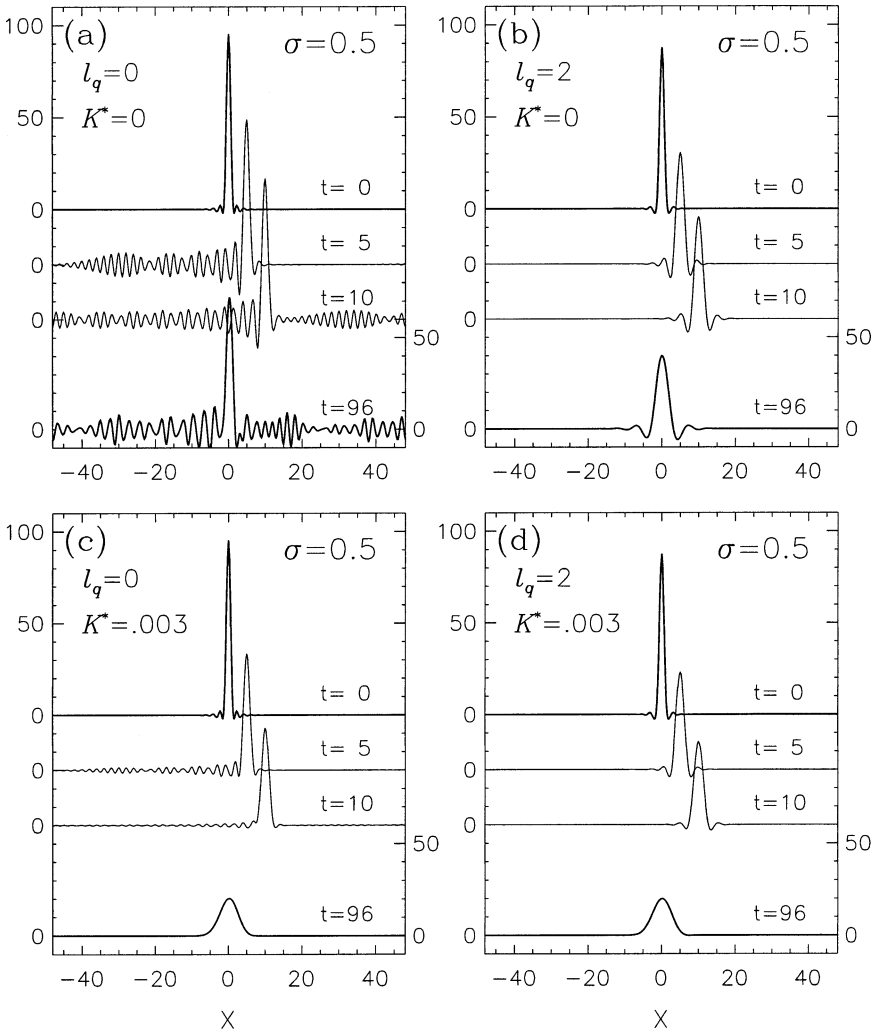

FIG. 8. Linear advection of a Gaussian peak, $\sigma = 0.5$, in the periodic domain, $x = [-48, 48]$. The four possible combinations of the DC filter ($l_q = 0$ or 2) and second-order diffusion ($K^* = 0$ or 0.003) are shown in (a)–(d).

wavelengths than those in FD. The fact that the maximum frequency attained by CST has a higher value at a shorter wavelength ($l = 2.7$) than those by FD is significant in domain nesting, since the transmissibility of waves across the interface requires the existence of matching frequencies on both the sides of the interface. The shorter waves to the left of the maximum ω are anomalous in that c and c_g have the opposite signs, and they are generated as backward spreading noise at the interface, when the normal longer waves of same ω cannot be transmitted across the interface.

The variation of phase speeds in the range of $\Delta t = 0.1$ to 0.4 is shown in Fig. 7c for CST with the DC filter and also without the filter. The filter reduces the dispersion of normally propagating waves; more importantly, as was discussed in section 5, the filter also reduces, very selectively, the amplitude of anomalous short waves.

b. Advection of Gaussian peaks

The linear properties of the CST method are further demonstrated in the advection of a Gaussian peak (the error function of unit height) with the standard deviation σ,

$$u(x) = e^{-x^2/(2\sigma^2)}, \tag{7.3}$$

by the equation with optional diffusion,

$$\partial_t u + c_0 \partial_x u = K \partial_{xx} u. \tag{7.4}$$

A periodic domain, $x = [-48, 48]$, is assumed with $\Delta x = 1$, $\Delta t = 0.1$, and $c_0 = 1$, so that the peak should return to the initial position in 960 time steps or at $t = 96$. Diffusion, in terms of the normalized coefficient (5.7), is set to either $K^* = 0$ or 0.003, and the DC filter to either $l_q = 0$ or 2. The four possible combinations of these options are shown in Figs. 8a–d for $\sigma = 0.5$, and in Figs. 9a–d for $\sigma = 2$. For ease of interpretation,

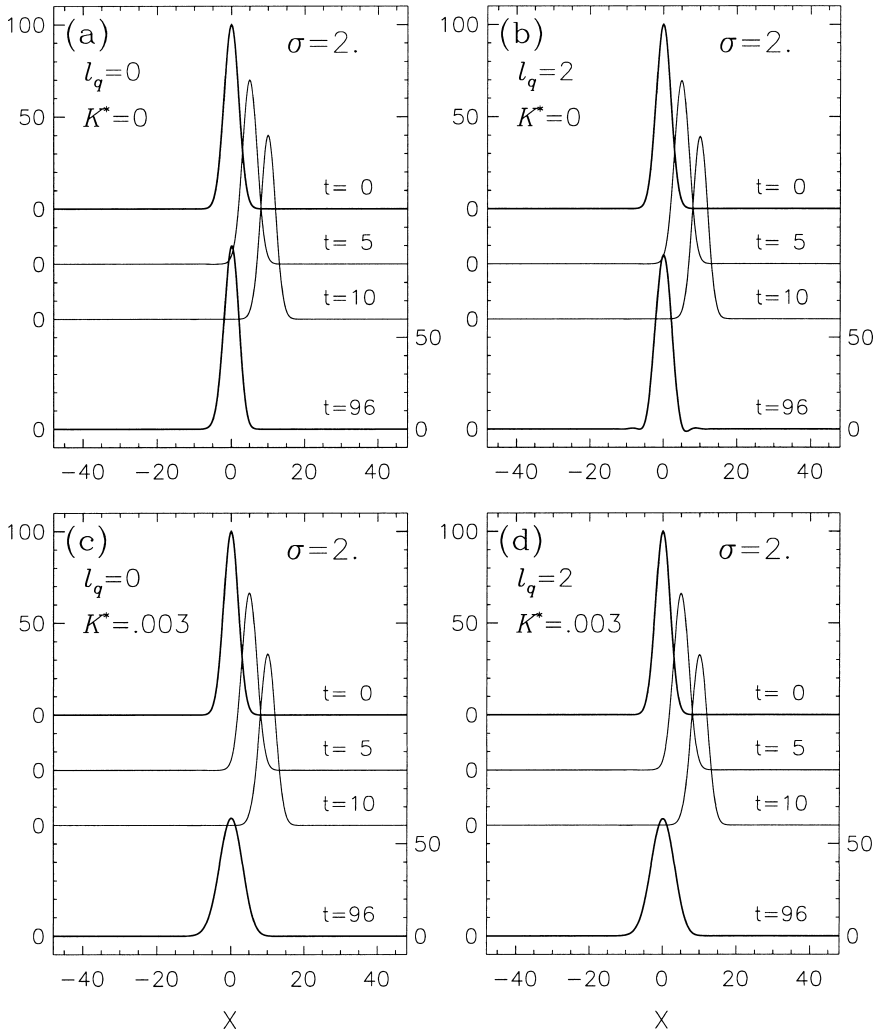

FIG. 9. The same as in Fig. 8 except for $\sigma = 2$.

the Fourier amplitudes of u are shown in Figs. 10a,b for both σ.

For the extremely narrow peak of $\sigma = 0.5$, the Fourier spectrum at $t = 0$ has significant amplitudes in short waves ($l < 2.7$) as shown in Fig. 10a. With neither the filter nor diffusion, the spectrum does not change with time, but, in the physical space, those short waves of negative group velocities rapidly spread backward as shown in Fig. 8a; at $t = 10$, they have already encircled the entire domain. On the other hand, the main spectral components ($l > 2.7$) propagate normally with little dispersion, so that the well-preserved peak arrives at the starting point exactly at $t = 96$.

With only the DC filter (Fig. 8b), the anomalous short waves are totally eliminated, but the sixth-order taper of the filter cuts the spectrum rather steeply (Fig. 10a), so that Gibbs's sidelobes become attached on both sides of the peak. When the diffusion alone is applied (Fig. 8c), it substantially reduces the anomalous waves though not as quickly as the DC filter, and its effect extends to far longer waves (Fig. 10a). Thus, the second-order taper of the diffusive filter does not generate sidelobes, but the height of the peak is significantly reduced, and the width broadened. When both the options are employed (Fig. 8d), the DC filter eliminates short waves and the diffusion removes Gibbs's sidelobes but only at the expense of longer waves in the desirable signal.

For the moderately broad peak of $\sigma = 2$, the Fourier spectrum (Fig. 10b) does not contain anomalous short waves at the start, and the CST method without the dissipative options, Fig. 9a, yields almost perfect advection. When the DC filter is applied (Fig. 9b), it eventually clips the tail of the spectrum, and small sidelobes appear at $t = 96$, although the main peak is barely affected. With diffusion (Figs. 9c,d), the height reduction and broadening of the peak are clearly noticeable.

In a demonstration of his ''local spectral (LS) method,'' Anderson (1989) shows an example of linear advection of the Gaussian peak with diffusion, which is equivalent, in our notation, to $\sigma = 3.54$ and $K^* =$

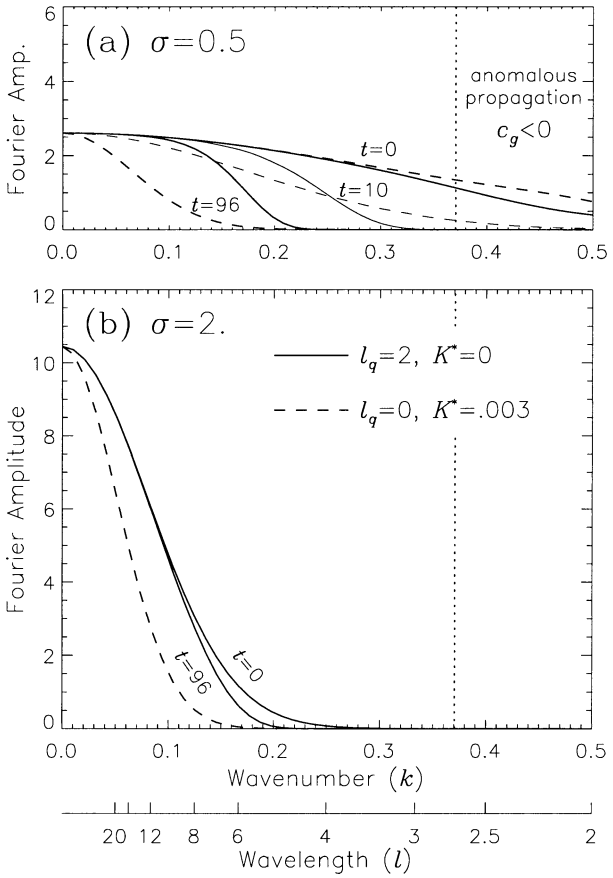

FIG. 10. The Fourier amplitude spectra of the advecting Gaussian peaks of (a) $\sigma = 0.5$ and (b) $\sigma = 2$; for the cases of DC only (solid) and diffusion only (dashed). Amplitudes in the range of anomalous propagation are responsible for rapidly retrograding noise in Figs. 8a,c.

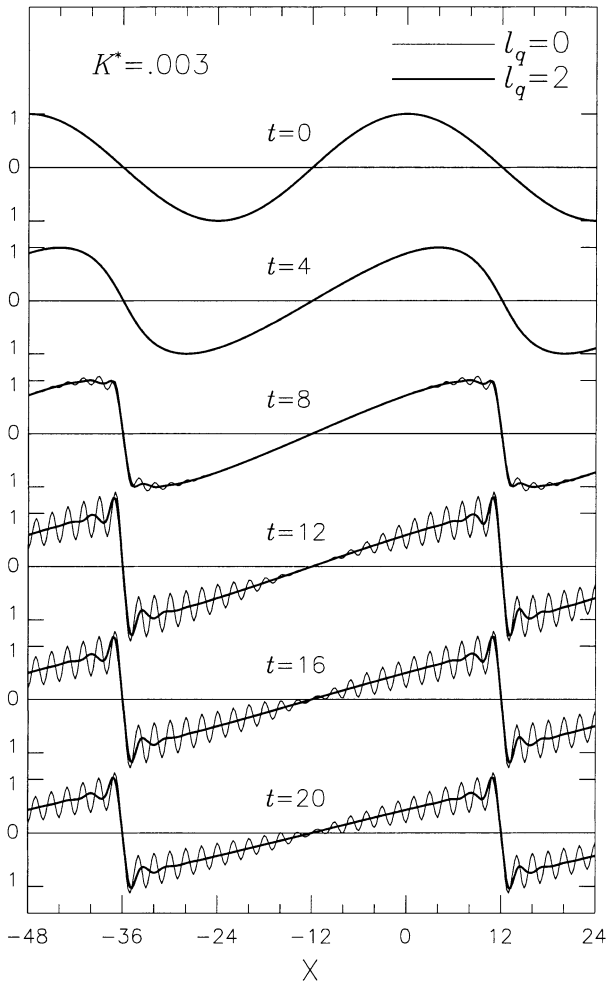

FIG. 11. The development with time of sawtooth waves in nonlinear advection, with the DC filter (thick lines) and without (thin lines); diffusion $K^* = 0.003$ in both cases.

0.012. For this σ but without diffusion, the present CST method will produce undamped, perfect advection, either with the DC filter or without.

8. Nonlinear advection

Following Anderson (1989), we now test the more challenging problem of nonlinear advection by

$$\partial_t u + u\partial_x u = K\partial_{xx} u, \tag{8.1}$$

in the same periodic domain, $x = [-48, 48]$, with $\Delta x = 1$ and $\Delta t = 0.1$, as before. The initial condition, however, is

$$u(x) = \cos(2\pi x/l_0), \tag{8.2}$$

where $l_0 = 48$. While the LF and AB schemes of time integration generate nearly identical results, those shown below are by the AB scheme in accordance with Anderson.

The development of the sawtooth wave with time is shown in Fig. 11, for the run with the DC filter (thick lines) and the run without (thin lines), but both the runs employ diffusion $K^* = 0.003$. The crest and trough of the initially symmetric wave gradually tilt toward the confluent point at $x = 12$; by the time $t = 8$, the tilt reaches the resolvable maximum and begins to generate anomalous short waves that rapidly spread backward unless they are immediately removed by the DC filter. The assumed K^*, which is for the MM5 background diffusion (section 5), is not large enough to suppress the continuously generated anomaly, although it does not worsen with time after the generation and dissipation reaches a near equilibrium.

Figure 12 compares the results of various values of K^*, all at $t = 16$. When the DC filter is absent (thin lines), the suppression of anomalous waves requires $K^* = 0.024$ or greater. If the filter is employed (thick lines), no such noise is present even with $K^* = 0$, except for Gibbs's sidelobes due to the sharp spectral cutoff. With increasing K^*, the sidelobes themselves are reduced in amplitude. Anderson's example (his Fig. 5 by the LS method) corresponds to $K^* = 0.012$.

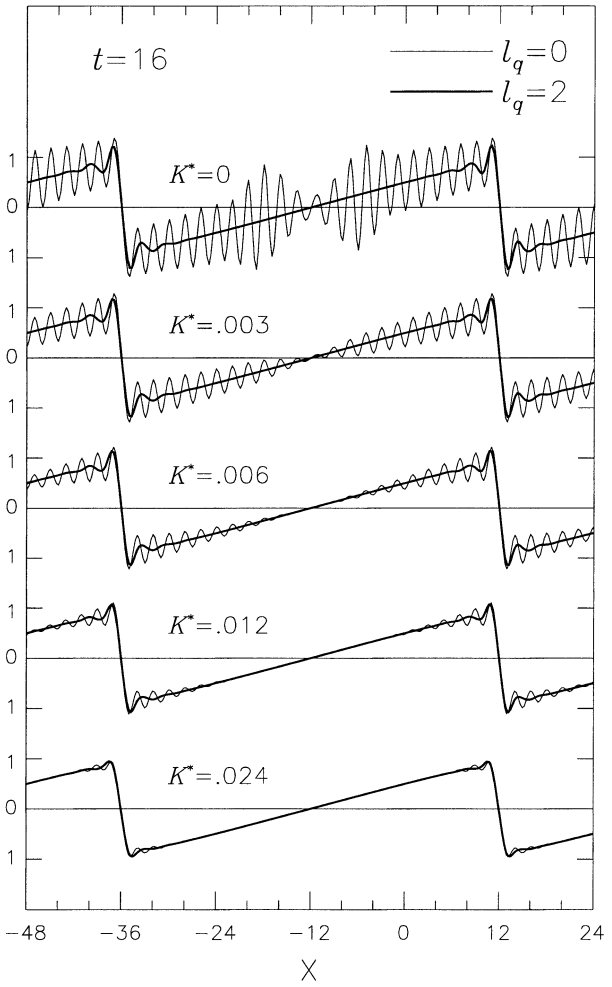

FIG. 12. The effects of various diffusivity, $K^* = 0$ to 0.024, on the sawtooth waves in nonlinear advection, with the DC filter (thick lines) and without (thin lines); all cases are shown at $t = 16$.

9. Open boundary conditions

a. Exiting advection

One of the advantages of the CST method is its ability to impose exact boundary conditions on the represented fields (section 3). While the choice of BC must be appropriate to the physical problem at hand, the act of imposition does not involve the physical equations themselves. This feature, which will be fully exploited in domain nesting, is demonstrated below in the simpler context of advection exiting through the open boundary of a finite domain. Both linear and nonlinear advection,

$$\partial_t u + c_0 \partial_x u = 0, \tag{9.1a}$$

$$\partial_t u + (c_0 + u)\partial_x u = K\partial_{xx} u, \tag{9.1b}$$

are discussed together, with $c_0 = 1$, $\Delta x = 1$, and $\Delta t = 0.1$. The DC filter, $l_q = 2$, is employed in both cases, but diffusion, $K^* = 0.012$, is assumed only in the nonlinear case (9.1b). The initial condition for u is given by the Gaussian peak (7.3) with $\sigma = 8$.

The domain $x = [-48, 48]$ is now finite, implying that, although the advection is supposed to continue beyond the outflow boundary at $x = 48$, calculations are made only within the domain. Since the CST method defines spatial derivatives at every point in the domain, including the boundary, there should be no need to constrain or modify the first-order equation at the outflow boundary. Therefore, the least invasive BC is R0, which positively asserts that no extraneous condition is imposed. No disturbance is supposed to come into the domain through the inflow boundary at $x = -48$, and this condition should positively be asserted by R2T10 or R3. In the present example, however, we assume R0 also at the inflow boundary, in order to test if the initial condition itself is sufficient for keeping the inflow boundary quiet, if not exactly at zero. The results of time integration are shown in Fig. 13 for the linear advection (solid lines) and the nonlinear (dash–dot lines). In both cases, the peaks move out of the domain as if there were no boundary, and the domain remains calm thereafter. Similar tests were performed with other BC options, such as R1T1 and R1T2, and the results (not shown) were nearly as perfect as with R0.

It should be noted, however, that the DC filter that eliminates anomalous short waves is critically important to the demonstrated results. If the filter is not employed, those anomalous waves reach the boundaries and generate varied reactions that are markedly dependent on the chosen BCs as well as on the scheme of time integration, LF or AB. On the other hand, Gibbs's sidelobes, which may be more pronounced for smaller σ, do not have any adverse effect on the outgoing advection. Gibbs's phenomena occur as the result of truncated short-wave components of an otherwise continuous spectrum. Thus, the advection of sidelobes is completely determined by the normal behavior of the remaining components that constitute the main peak.

b. Exiting gravity waves of mixed modes

In a number of limited-area gridpoint models (e.g., Orlanski 1976; Miller and Thorpe 1981), the outflow conditions were based on the Sommerfeld radiation condition that presumed one typical outflow velocity. In more general applications, however, there is more than one characteristic speed due to multimodal gravity waves in addition to advection, and the condition that depends on one mode may not be satisfactory for other modes. Such ambivalence is absent in the CST method, since our conditions are not adjusted to a particular solution but chosen for the domain. For the purpose of demonstration, we consider below the linearized shallow-water equations for two layers of incompressible fluid of different densities, ρ_1 for the lower layer, ρ_2 for the upper, and their ratio $r = \rho_2/\rho_1 < 1$. For simplicity, the same thickness H is assumed for the undisturbed state of each layer.

For the perturbed thickness and velocity of the lower

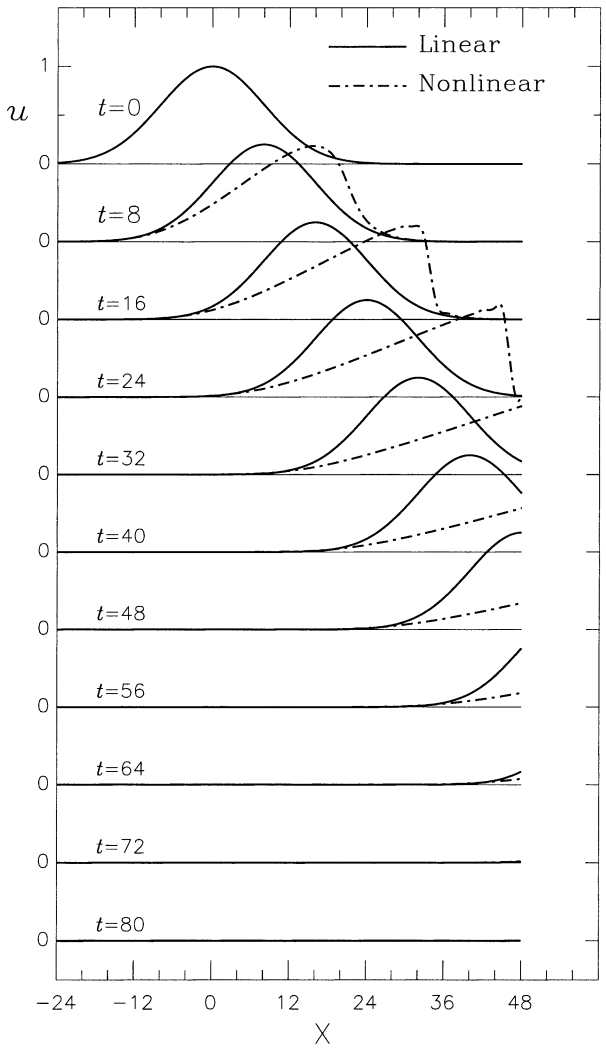

FIG. 13. Linear (solid) and nonlinear (dotted–dashed) advection of Gaussian peaks ($\sigma = 4$) through the open boundary at $x = 48$. Boundary conditions are R0 at both $x = 48$ and -48, although the inflow-end quarter of the domain is not shown.

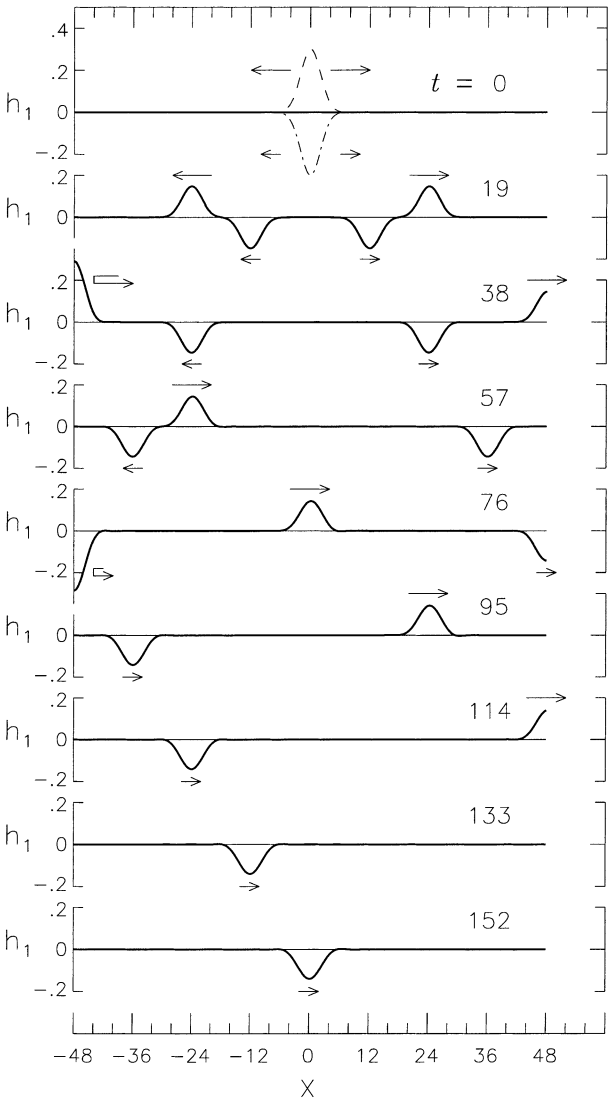

FIG. 14. The height deviations h_1 of gravity waves at the internal surface of a two-fluid system (linear shallow-water equations). A solid wall is assumed at $x = -48$, while the boundary is open at $x = 48$. At $t = 0$, only the top free surface (not shown) is disturbed, and the external mode (dashed) and internal mode (dotted–dashed) cancel each other at the internal surface. As time goes on, the two modes split into two fast-moving peaks and two slow-moving dips; the left-moving peak and dip are reflected at the solid wall, and the right-moving ones cleanly exit at the open boundary.

layer, h_1 and u_1, and those of the upper layer, h_2 and u_2, the equations are

$$\begin{aligned} \partial_t h_1 + H\partial_x u_1 &= 0, \\ \partial_t h_2 + H\partial_x u_2 &= 0, \\ \partial_t u_1 + g\partial_x(h_1 + rh_2) &= 0, \\ \partial_t u_2 + g\partial_x(h_1 + h_2) &= 0, \end{aligned} \tag{9.2}$$

where g is the acceleration of gravity. Although the four equations of (9.2) are integrated together as PEs of section 6, the solution may be interpreted as the sum of two normal mode solutions, the external (e) and internal (i) modes, so that we may write $h_1 = h_{1e} + h_{1i}$ and $h_2 = h_{2e} + h_{2i}$, where

$$\begin{aligned} h_{1e} &= (h_1 + rh_2)/2, \qquad h_{2e} = h_{1e}/r, \\ h_{1i} &= (h_1 - rh_2)/2, \qquad h_{2i} = -h_{1i}/r, \end{aligned} \tag{9.3}$$

with similar decompositions for u_1 and u_2. The phase speeds of the two modes are distinct and given, with $C \equiv (gH)^{1/2}$, by

$$c_e = \pm(1 + r)^{1/2}C, \qquad c_i = \pm(1 - r)^{1/2}C. \tag{9.4}$$

The example shown in Fig. 14 is for the choice $C = 1$ and $r = 0.6$, so that the ratio of c_e to c_i is exactly 2; calculations are made with $\Delta x = 1$ and $\Delta t = 0.1$ in a

finite domain $x = [-48, 48]$, which is open at the right but closed by a ''solid wall'' at the left; thus, the assumed BCs at $x = 48$ are R0 for both h and u, but the BCs at $x = -48$ are R1T1 (symmetry) for h and R2T20 (antisymmetry) for u. In the initial state, the fluids are at rest and only the free surface, $h_1 + h_2$, is raised in the shape of a Gaussian peak, or more specifically, $\sigma = 2$, and

$$h_2 = e^{-x^2/(2\sigma^2)}, \qquad h_1 = u_1 = u_2 = 0. \tag{9.5}$$

The result of time integration is shown in Fig. 14 in terms of h_1, the deviation of the internal surface. At $t = 0$, h_1 is identically 0 as assumed but it can be interpreted as the mutual cancellation of h_{1e} (dashed) and h_{1i} (dotted–dashed). As time increases, both the modes split into the right- and left-propagating components at the speeds that depend on the modes; thus at $t = 19$, the two fast-moving peaks of h_{1e} and the two slow-moving dips of h_{1i} are individually manifest on the profile of h_1. At $t = 38$ (or, 37.95 to be exact), the right-moving peak of h_{1e} is exiting the open boundary, while the left-moving peak is being reflected by the solid wall; exactly the same fate is experienced at $t = 76$ by the slow-moving dips of h_{1i}. The reflected peak of h_{1e} exits the open boundary at $t = 114$, and the final dip of h_{1i} will exit (not shown) at $t = 228$.

Although the clean exit of outgoing signals has been demonstrated above, (9.4) supports propagation in two directions even at the boundary, implying that ''outgoing'' is not an inherent property of the boundary but the nature of the particular signal in these hyperbolic wave equations. In fact, when the nonlinear version of (9.2) was integrated, small numerical residues that were left behind by the exiting main signal turned into a false inflow (left propagating) signal of very large spatial scale. The homogeneous BCs, such as R0 or R1T2, could not keep the slow ''infrared'' creep from spreading over the domain, although R1T1 for both h and u did in the nonlinear case. In realistic applications in which actual signals simultaneously travel in all directions, the above example of an isolated finite domain is rather irrelevant, and nested domains connected by inhomogeneous conditions must be considered.

10. Concluding remarks

The concept and formalism of the cubic-spline transform (CST) method, which was also known by another acronym SAFER (spectral application of finite-element representation), have been presented and tested in application to the advection and gravity-wave equations in a single domain. A theoretical error analysis is also found in the appendix.

The CST method is designed for the express purpose of application to nested models of the atmosphere. The characteristic features of the method—the ease of implementing boundary conditions, the substantially reduced shortwave dispersion, and the optional built-in low-pass filter—will prove extremely valuable for the design of a domain-nesting strategy in which the broadest possible bandwidth is desired in noise-free two-way communication across the interfaces.

In the actual procedure of nesting, there are additional problems to consider. One of them is the placement of the three transforms, SA, SB, and SI, as well as the model payload, PE, within the scheme of stepping up (fine to coarse) and down (coarse to fine) the logistic ladder of domains. For the algebraically exact rule of basis conversion, it turns out to be most logical (and practical) that the SI–PE–SB trio is chained in the up-ladder sequence, and that SA is chained in the down-ladder sequence. Another is the question of how to define the minimization integral when a domain (except for the innermost) contains a subdomain. If the whole subdomain is included in the integral, a subtle but potentially disastrous interaction can occur between Gibbs's sidelobes and the inhomogeneous interface conditions. A similar, though unrelated, question about the subdomain also arises in solving the elliptic equation for semi-implicit acoustic adjustment.

The theoretical foundation of the CST method and its applied procedure for nesting are extendable to multidimensional space without much alteration. Computational efficiency, however, is highly dependent on the numerical algorithm for the SA transform, especially on the utilization of bandedness in matrix operations. In a vertical 2D model, the minimization integral can be factorized, and the bandedness both in x and z dimensions is independently utilized. In a horizontal 2D model, thus also in 3D, factorization of the x and y dimensions is not possible, and our current algorithm only partially utilizes the second bandedness.

These and other particular problems of nesting will be discussed in a subsequent paper.

Acknowledgments. The author would like to thank Dr. H. E. Willoughby, the director of the Hurricane Research Division, and Howard Friedman, for support of this work, and Dr. George Soukup for improving the manuscript. The helpful comments and suggestions from Drs. Wayne Schubert and Mark DeMaria, and also those by an anonymous reviewer, are gratefully acknowledged.

APPENDIX

Fourier Analysis of the Cubic-Spline Representation

a. Fourier coefficients

Any periodic test function $\check{f}(x)$, which is defined in the primary domain $[0, D]$, may be represented by $f(x)$, a complex Fourier series:

$$f(x) = \sum_{j=-\infty}^{\infty} F(j) e^{i2\pi jx/D}, \tag{A.1}$$

where j is an integer (j/D the wavenumber) and i is the imaginary unit. The Fourier coefficients $F(j)$ are determined by

$$F(j) = \frac{1}{D}\int_0^D \breve{f}(x)e^{-i2\pi jx/D}\,dx. \qquad \text{(A.2)}$$

b. Waves on grid points

As a basis of comparison, let us first review the familiar case of harmonic waves that are represented only at the discrete grid points $x_m = m\Delta x$, where $\Delta x = D/\overline{m}$ and $m \in \{0, 1, 2, \ldots, \overline{m} - 1\}$. The test function $\breve{g}_n(x)$ for any integer n is given, in the Dirac comb notation, by

$$\breve{g}_n(x) = \Delta x \sum_{m=0}^{\overline{m}-1} \delta(x - x_m)e^{i2\pi nx/D}, \qquad \text{(A.3)}$$

and its Fourier coefficients are

$$G_n(j) = \frac{1}{\overline{m}}\sum_{m=0}^{\overline{m}-1} e^{i2\pi(n-j)m/\overline{m}} = \delta(n, j; \overline{m}), \qquad \text{(A.4)}$$

where

$$\delta(n, j; \overline{m}) \equiv \begin{cases} 1 & \text{if } n - j = 0 \bmod(\overline{m}). \\ 0 & \text{otherwise.} \end{cases} \qquad \text{(A.5)}$$

Note that (A.5) is a variation of Kronecker's delta that allows the two indices to differ by multiples of $\overline{m}$.

Since (A.3) comprises $\overline{m}$ discrete data, only $\overline{m}$ coefficients $G_n(j)$ for each n are linearly independent. Thus, the Fourier representation of $\breve{g}_n(x)$ must be a finite Fourier series,

$$q_n(x) = \sum_{j=-\overline{m}/2+1}^{\overline{m}/2} G_n(j)e^{i2\pi jx/D}, \qquad \text{(A.6)}$$

where the summation is taken over the ''main band'' $-\overline{m}/2 + 1 \le j \le \overline{m}/2$ (for even $\overline{m}$). Within this range, (A.5) selects one nontrivial value of j for each n. As for the range of n, though it is unlimited, there is no practical need to look outside $-\overline{m} < n < \overline{m}$.

While the integer wavenumbers n and j for the domain are mathematically convenient, the fractional wavenumber k, defined over the grid or nodal interval Δx, is more directly focused on the problems of representation, so that the input and output wavenumbers may be denoted by

$$k_{\text{in}} = n/\overline{m}, \qquad k_{\text{out}} = j/\overline{m}. \qquad \text{(A.7)}$$

The Fourier spectral response may also be expressed by $R(k_{\text{in}}, k_{\text{out}}) = |G_n(j)|$. For further convenience of discussion, let the complementary pair of wavenumbers, k and $k' = 1 - k$, represent the resolvable and unresolvable ranges of waves, respectively, which are defined numerically by

$$0 < k \le 0.5 \le k' < 1. \qquad \text{(A.8)}$$

The inverse, $l = 1/k$ or $l' = 1/k'$, is the wavelength in units of Δx. Note that $k = k' = 0.5$ is the Nyquist wavenumber. In the new notation, the nontrivial response mentioned in the preceding paragraph can explicitly be stated as

$$k_{\text{in}} = \begin{cases} k \to k_{\text{out}} = k, & R_o \equiv R(k, k), \\ k' \to k_{\text{out}} = -k, & R_a \equiv R(k', -k), \end{cases} \qquad \text{(A.9)}$$

for positive k_{in}, and is also illustrated in Fig. A1a; the response R_o is ordinary, while R_a is aliased in that an input at *unresolvable* k' erroneously produces an output at *resolvable* $-k$. (This is the reason why k' is called unresolvable.)

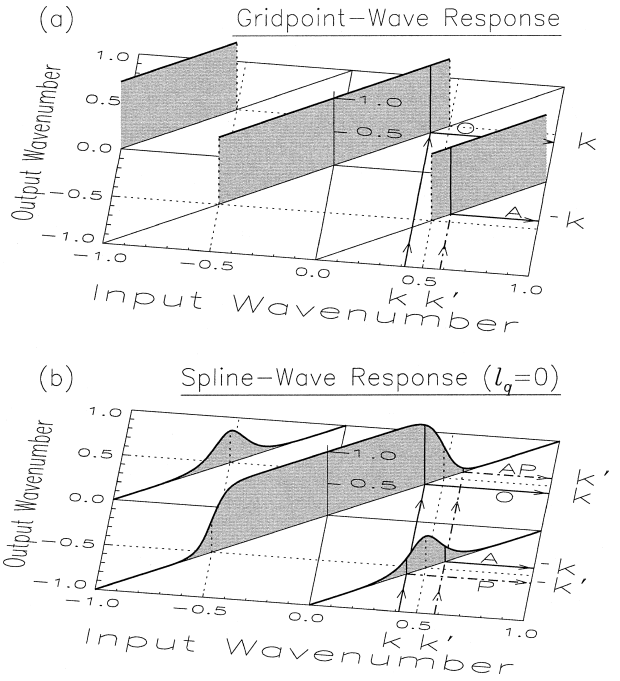

FIG. A1. Fourier spectral responses of (a) gridpoint representation and (b) cubic-spline representation (no DC filter). The arrowed paths connect the complementary pair of input wavenumbers, k (solid) and k' (dotted–dashed), with the output wavenumbers, which may be either k or k' (with sign). The label, O, A, P, or AP, on the output paths indicates the ordinary, aliased, parasitic, or aliased-parasitic responses, respectively. The dotted lines mark the Nyquist wavenumber.

c. Waves by cubic-splines

The Fourier analysis of spline-represented harmonic waves is a little more complicated due to the fact that two integral transforms are performed: the cubic-spline transforms, described in the text (section 4), convert the test function $\breve{u}_n(x) = \exp(i2\pi nx/D)$ to its cubic-spline representation $u_n(x) = \text{SI}[\text{SA}[\text{SB}[\breve{u}_n]]]$, and the latter is then taken to be the input $\breve{f}_n(x)$ to the Fourier transform (A.2) that determines $F_n(j)$. For this purpose, the domain must be periodic, and the cubic-spline transforms, below, are given in the closed form under the periodicity condition.

Two salient facts about the periodic domain may be noted. The first is a simple relationship of the Fourier coefficients $\Phi_m(j)$ of the basis function $\tilde{\phi}_m(x)$ at any node m to those at node 0. Namely, since $\tilde{\phi}_m(x) = \tilde{\phi}_0(x - m\Delta x)$,

$$\Phi_m(j) = \frac{1}{D}\int_0^D \tilde{\phi}_m(x)e^{-i2\pi jx/D}\,dx = \Phi_0(j)e^{-i2\pi jm/\overline{m}}. \quad \text{(A.10)}$$

The second fact, assuming a constant weight for the derivative constraint, is that the matrix elements of $\tilde{\mathbf{P}} + \tilde{\mathbf{Q}}$, as well as those of $\tilde{\mathbf{I}} \equiv (\tilde{\mathbf{P}} + \tilde{\mathbf{Q}})^{-1}$, are invariant in the direction parallel to the diagonal. Thus, if m and m' are the row and column indices and $m'' \equiv m' - m$ (mod $\overline{m}$) is the cross-diagonal index, $\tilde{I}_{mm'} = \tilde{I}_{m,m+m''}$ is a function of m'' only.

The SB transform of $\breve{u}_n(x)$ gives

$$\tilde{b}_m = \int_0^D \tilde{\phi}_m(x)e^{i2\pi nx/D}\,dx = D\Phi_0(-n)e^{i2\pi nm/\overline{m}}, \quad \text{(A.11)}$$

which is transformed further by SA and SI to yield

$$\breve{f}_n(x) \equiv u_n(x) = D\Phi_0(-n)\sum_{m=0}^{\overline{m}-1}\left[\tilde{\phi}_m(x)\sum_{m'=0}^{\overline{m}-1}\tilde{I}_{mm'}e^{i2\pi nm'/\overline{m}}\right], \quad \text{(A.12)}$$

which is Fourier transformed to yield

$$F_n(j) = D\Phi_0(-n)\Phi_0(j)\sum_{m=0}^{\overline{m}-1}\sum_{m'=0}^{\overline{m}-1}\tilde{I}_{mm'}e^{i2\pi(nm'-jm)/\overline{m}}. \quad \text{(A.13)}$$

By switching the double summation w.r.t. (m, m') to that w.r.t. (m, m''), and noting that

$$C(n) \equiv D\overline{m}\sum_{m''=0}^{\overline{m}-1}\tilde{I}_{m,m+m''}e^{i2\pi nm''/\overline{m}} \quad \text{(A.14)}$$

is independent of m, we arrive at

$$F_n(j) = \Phi_0(-n)\Phi_0(j)C(n)\delta(n, j; \overline{m}). \quad \text{(A.15)}$$

As for the input wavenumbers n, it is again sufficient to consider the range $-\overline{m} < n < \overline{m}$. On the other hand, unlike $\breve{g}_n(x)$, the spline-represented test function $\breve{f}_n(x)$ is continuously defined in the domain, so that its Fourier coefficients for each n are independently defined in the infinite range of j. However, since $\Phi_0(j)$ rapidly decreases to zero for large $|j|$, the examination of $F_n(j)$ can be safely limited to a finite range, say, $-\overline{m} < j < \overline{m}$. Within this range, (A.5) selects nontrivial responses at two values of j for each n. In terms of the fractional wavenumbers defined in (A.7) and (A.8), the nontrivial responses $R(k_{\text{in}}, k_{\text{out}}) = |F_n(j)|$ are found in four categories,

$$k_{\text{in}} = \begin{cases} k \to k_{\text{out}} = \begin{cases} k, & R_o \equiv R(k, k), \\ -k', & R_p \equiv R(k, -k'), \end{cases} \\ k' \to k_{\text{out}} = \begin{cases} -k, & R_a \equiv R(k', -k), \\ k', & R_{ap} \equiv R(k', k'), \end{cases} \end{cases} \quad \text{(A.16)}$$

and are also illustrated in Fig. A1b for the case of $l_q = 0$ (no DC filter). The ordinary and aliased responses, R_o and R_a, respectively, are the same categories as in (A.9), though their magnitudes, especially that of R_a, are significantly different; the two new categories R_p and R_{ap} are explained below.

d. Effects of the DC filter on representation errors

When $k_{\text{in}} = k$ in the *resolvable* range, the main response is R_o at the same k. However, since the harmonic test function $\breve{u}_n(x)$ is not in S_3, the cubic-spline function $u_n(x)$ necessarily contains other *parasitic* harmonics, of which R_p at $-k'$ is the major component. The other parasitic components are, at least, two orders of magnitude smaller than R_p and may be ignored. As shown in Fig. A1b, R_p itself is negligibly small for $k \lesssim 0.25$ or $l \gtrsim 4$. As k increases toward 0.5, k' decreases toward the same value, and $u_n(x)$, which is the sum of the ordinary and parasitic waves, will appear as modulated waves. Figure A2 illustrates the spatial realization of these waves for the real (cosine) test functions at $k =$ 0.458, 0.333, and 0.25 ($l =$ 2.18, 3, and 4).

When $k_{\text{in}} = k'$ in the unresolvable range, its main response is the aliased R_a at $-k$, accompanied by its own parasitic harmonic, R_{ap} at k'.

Although we have called k' unresolvable, the parasitic components in the cubic-spline representation are actually present in space as shown in Fig. A2. The spatial phases of the parasites, however, are more strongly tied to the discrete nodes than the ordinary components, and create an appearance of uneven propagation of short waves ($l \lesssim 3$); in the limit of $l = 2$, the wave cannot move between the nodes. On the other hand, far more damaging consequences may follow from R_a, if nonlinear processes of the model continually generate a spectral input at unresolvable scales that are erroneously aliased to resolvable scales. In order to ameliorate these representational errors, the SA transform normally includes a built-in DC filter (section 5). The Fourier spectral responses in the case of the filtered SA ($l_q = 2$) are shown for one application (Fig. A3a) and 10 repeated applications (Fig. A3b). When compared with the case of no filter in Fig. A1b, the effectiveness of the DC filter is evident in reducing or eliminating both the parasitic and aliased responses. It is inevitable that the filter also reduces the ordinary response R_o of short waves. Nevertheless, as was discussed in section 5, the loss of response due to the DC filter is limited to a much narrower range near the Nyquist scale than are similar losses that

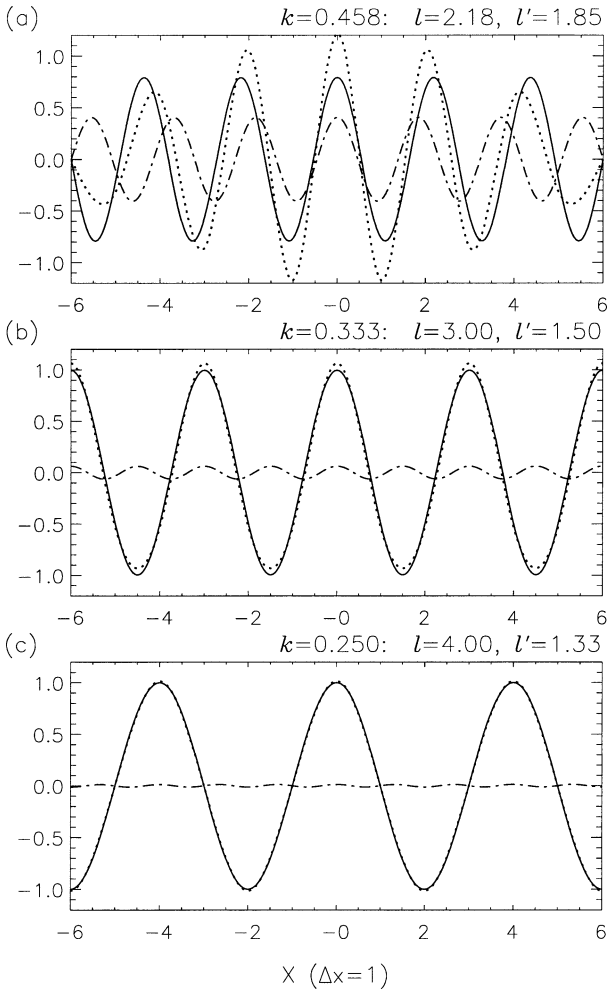

FIG. A2. Examples of the parasite in short waves (no DC filter) for the input wavelengths: (a) $l = 2.18$, (b) 3, and (c) 4. In each panel, the solid line is the ordinary response, the dotted–dashed line the parasite, and the dotted line the modulated total response.

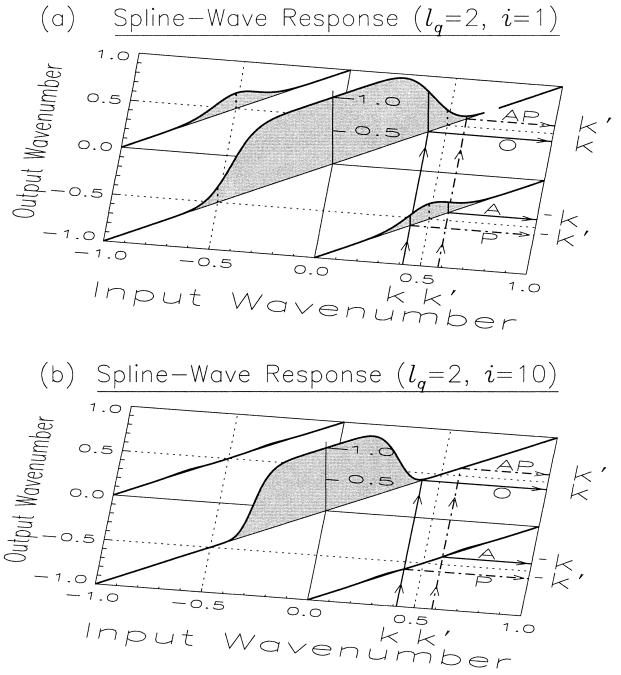

FIG. A3. Fourier spectral responses of the cubic-spline representation with the DC filter ($l_q = 2$): (a) 1 iteration and (b) 10 iterations. Compare Fig. A1b with no DC.

would be incurred by the use of customary diffusion operators.

e. Effects of reduced sampling in the SB transform

In the theoretical discussion above, both the Fourier and SB transforms have been presented as integral transforms. In order to produce the results shown in Figs. A1b and A3a,b (for $\overline{m} = 96$), the Fourier transform (A.2) was calculated by the FFT with $4\overline{m}$ sampling points, and the SB transform by the fifth-degree ($\overline{\mu} = 5$) Gaussian quadrature (section 4c). Thus, all the curves in the figures are quite accurate depictions of the theoretical results. In practical applications of the spline transforms, however, it is tempting to employ a smaller value of $\overline{\mu}$, since the amount of calculation in most computational blocks in Fig. 6, except for the SA transform, is proportional to $\overline{\mu}$ (per spatial dimension). Therefore, it is important to assess the increased risk of misrepresentation that a reduced $\overline{\mu}$ may incur.

The Fourier spectral responses in the case of $\overline{\mu} = 3$ are shown in the upper row of Fig. A4, for $l_q = 0$ (panel a), $l_q = 2$ (panel b), $l_q = 2$ (10 times) (panel c). The results are nearly identical to the corresponding responses shown in Figs. A1b and A3a,b, except for a very small increase ($\lesssim 0.022$) in R_a at $k_{\text{in}} \gtrsim 0.75$. The case of $\overline{\mu} = 2$ is similarly shown in Figs. A4d–f, in the lower row. While changes in R_o and R_p are again insignificant, the increase in R_a is now conspicuous, and the DC filter, even repeated, is ineffective for reducing R_a at $k_{\text{in}} \gtrsim 0.6$, although the residual value ($\lesssim 0.24$) is much smaller than the full aliasing in the case of the gridpoint method.

Even if R_a does not vanish exactly, the actual risk of aliasing depends on the rate of spectral input in the *unresolvable* range. If the main cause of such input is quadratic products of prognostic variables in the physical equations, the input at $k_{\text{in}} \gtrsim 0.6$ can be suppressed by maintaining the resolvable spectra of the variables well filtered at $k \gtrsim 0.3$ ($l \lesssim 3$). Therefore, it is possible to use $\overline{\mu} = 2$ and still achieve a substantially alias-free integration of nonlinear models, although it is prudent to run a few comparison tests with $\overline{\mu} = 3$ for each new physical problem; the need for greater values of $\overline{\mu}$ is highly unlikely. All the experiments demonstrated in Ooyama (2001) were performed with $\overline{\mu} = 2$.

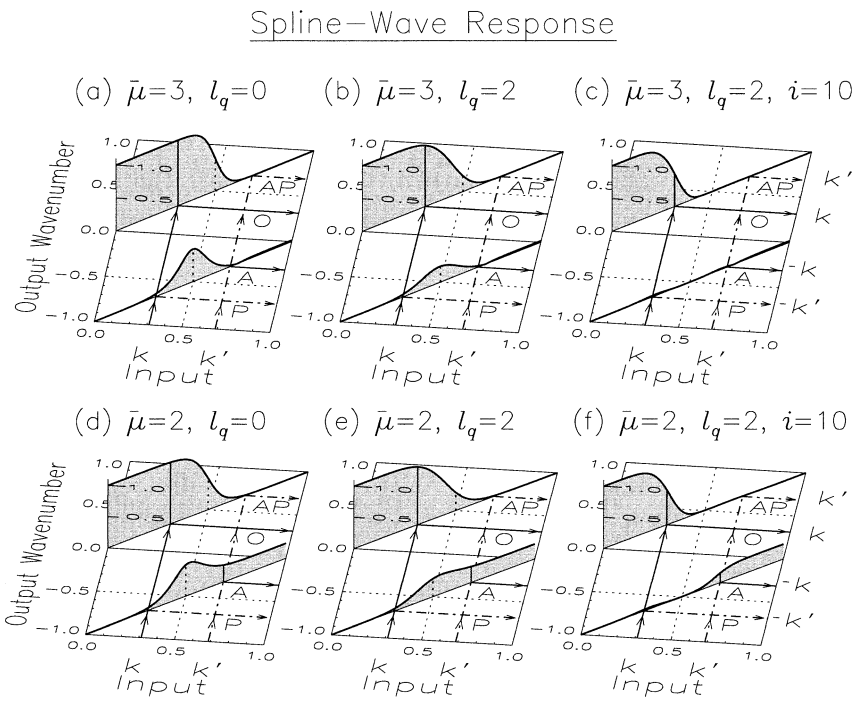

FIG. A4. The effects of discrete sampling in the SB transform by $\overline{\mu}$th-degree Gaussian quadrature: the first row [(a)–(c)] for $\overline{\mu} = 3$, and the second row [(d)–(f)] for $\overline{\mu} = 2$. The further effects of the DC filter are shown by three panels of each row: no filter, filtered once, and filtered 10 times, respectively.

f. The rate of convergence

In application of discretized numerical methods, the approximate solutions should converge to the ''true'' solution of a given problem, when the resolution, or Δx, is arbitrarily refined. Thus, Ooyama (2001) demonstrated such convergence of the CST method in a nonlinear simulation of a density current, a test problem that was specifically designed for the purpose (Straka and Anderson 1993). In more general applications, however, there is a practical limit to reducing Δx, and it is often necessary to adjust dissipative mechanisms, either physical or computational, in order to avoid catastrophic accumulation of numerical errors near the resolution limit for a chosen Δx. Therefore, our emphasis in the preceding discussion was to understand the behavior of the cubic-spline representation near the Nyquist scale. For completeness of the analysis, we shall now discuss the rate of convergence of the representation with increasing resolution.

If $\breve{f}(x)$ in (A.2) is twice differentiable but its third-order derivative is piecewise continuous, it can be shown (e.g., Gottlieb and Orszag 1977) that the partial sum for $|j| \le \overline{m}$ on the rhs of (A.1) will converge to the infinite sum, with their difference decreasing like $O(\overline{m}^{-4})$ as $\overline{m} \to \infty$. Therefore, if $\breve{f}(x)$ is a cubic-spline function for $\Delta x = D/\overline{m}$, its finite Fourier representation is not likely to converge faster than $O(\overline{m}^{-4})$ as $\overline{m} \to \infty$, or $O(\Delta x^4)$ as $\Delta x \to 0$. Although this conclusion is essentially correct, the argument is weak, since it only refers to the presence of a third-order discontinuity but ignores the fact that the number of points of such discontinuity also increases with $\overline{m}$.

A more direct proof of convergence that specifically accounts for the cubic-spline transform is obtained by comparing the Fourier coefficients of $\breve{u}_n(x) = \exp(i2\pi nx/D)$ with those of $u_n(x) = \mathrm{SI}[\mathrm{SA}[\mathrm{SB}[\breve{u}_n]]]$, where n is an integer. For the former, $\breve{f} = \breve{u}_n$, (A.2) gives $\breve{F}_n(j) = \delta(n - j)$, for which the inverse transform (A.1) exactly returns $\breve{u}_n$; and for the latter, $\breve{f} = u_n$, (A.15) shows $F_n(j)$, for which the inverse transform yields an approximation to $\breve{u}_n$. Therefore, the error due to the cubic-spline transforms may be measured in terms of the difference between $\breve{R}(k_{\mathrm{in}}, k_{\mathrm{out}}) = |\breve{F}_n(j)|$, and $R(k_{\mathrm{in}}, k_{\mathrm{out}}) = |F_n(j)|$, where $k_{\mathrm{in}} = n/\overline{m} = n\Delta x/D$ and $k_{\mathrm{out}} = j/\overline{m} = j\Delta x/D$ are the input and output wavenumbers, normalized with respect to Δx.

As shown in (A.16), $R(k_{\mathrm{in}}, k_{\mathrm{out}})$ is nontrivial only at a few pairs of k_{in} and k_{out}, and, for the convergence question at sufficiently large $\overline{m}$, we only need to consider the ordinary response, $R_o = R(k_{\mathrm{in}}, k_{\mathrm{in}})$, and the parasitic response, $R_p = R(k_{\mathrm{in}}, k_{\mathrm{in}} - 1)$, for $0 < k_{\mathrm{in}} < 0.5$. As for the exact Fourier transform, $\breve{R}_o = \breve{R}(k_{\mathrm{in}}, k_{\mathrm{in}}) = 1$ is the only response. Thus, the error of the cubic-spline representation at $\overline{m} \gg n$, for a given n, is represented by the two measures,

$$E_o(k_{\mathrm{in}}) = 1 - R_o \quad \text{and} \quad E_p(k_{\mathrm{in}}) = R_p, \qquad \text{(A.17)}$$

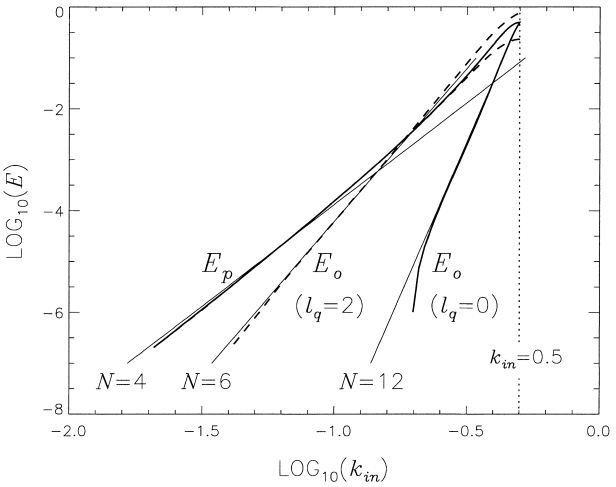

FIG. A5. The convergence of the cubic-spline representation with increasing resolution is demonstrated by the log–log diagram of the Fourier response errors, E_o (ordinary) and E_p (parasitic), vs $k_{in} = n\Delta x/D$, for $k_{in} < 0.5$. Since the wavenumber n/D of the test wave is fixed in this interpretation, $k_{in} \to 0$ implies $\Delta x \to 0$. Solid lines are for the case with no DC filter, and dashed lines with the DC filter ($l_q = 2$). (E_p at small k_{in} is not affected by the filter.) The slope $N = 4$, 6, or 12, of the thin straight lines suggests the order of error reduction as $\Delta x \to 0$.

and both are plotted in the log–log diagram in Fig. A5, with solid lines for $l_q = 0$ (no DC) and dashed lines for $l_q = 2$ (with DC); thin staight lines represent the slope $N = 4$, 6, and 12, as labeled. Thus, if we disregard slight deviations due to the loss of significant digits in calculation, the overall error of the cubic-spline representation decreases like $O(\Delta x^4)$ as $\Delta x \to 0$, in agreement with the earlier simple argument. This rate of convergence is solely due to the slow rate of the parasitic response whose output wavelength nearly equals Δx, regardless of how small Δx would become. As for the ordinary response, the rate of convergence is $O(\Delta x^{12})$ without the DC filter, or $O(\Delta x^6)$ with the sixth-order tapered DC filter.

The order of accuracy in this discussion is a global measure obtainable by the least squares fitting and does not directly relate to the order of local accuracy that is deduced in finite-difference methods by a Taylor expansion. In the latter sense, the CST method is much more accurate than the sixth-order finite-difference method in application to the linear advection equation (section 7a).

REFERENCES

Anderson, J. R., 1989: A local, minimum aliasing method for use in nonlinear numerical models. *Mon. Wea. Rev.*, **117,** 1369–1379.

Asselin, R., 1972: Frequency filter for time integrations. *Mon. Wea. Rev.*, **100,** 487–490.

Burridge, D. M., 1975: A split semi-implicit reformulation of the Bushby–Timpson 10-level model. *Quart. J. Roy. Meteor. Soc.*, **101,** 777–792.

Chen, C., 1991: A nested grid, nonhydrostatic, elastic model using a terrain-following coordinate transformation: The radiative-nesting boundary conditions. *Mon. Wea. Rev.*, **119,** 2852–2869.

Cullen, M. J. P., 1979: The finite element method. *Numerical Methods Used in Atmospheric Models*, Vol. II, GARP Publication Series, No. 17, GARP/WMO-ICSU Joint Organizing Committee, 300–337.

Davis, P. J., and I. Polonsky, 1964: Numerical interpolation, differentiation, and integration. *Handbook of Mathematical Functions*, M. Abramowitz and I. A. Stegun, Eds., National Bureau of Standards, 875–924.

de Boor, C., 1987: *A Practical Guide to Splines.* Applied Mathematical Sciences, No. 27, Springer-Verlag, 392 pp.

DeMaria, M., S. D. Aberson, K. V. Ooyama, and S. J. Lord, 1992: A nested spectral model for hurricane track forecasting. *Mon. Wea. Rev.*, **120,** 1628–1643.

Fulton, S. R., and W. H. Schubert, 1987: Chebyshev spectral methods for limited area models. Part I: Model problem analysis. *Mon. Wea. Rev.*, **115,** 1940–1953.

Golub, G. H., and C. F. Van Loan, 1996: *Matrix Computations.* 3d ed. Johns Hopkins University Press, 694 pp.

Gottlieb, D., and S. A. Orszag, 1977: *Numerical Analysis of Spectral Methods: Theory and Applications.* SIAM, 172 pp.

Grell, G. A., J. Dudhia, and D. A. Stauffer, 1995: A description of the fifth-generation Penn State/NCAR mesoscale model (MM5). NCAR Tech. Note. NCAR/TN-398+STR, 122 pp.

Juang, H.-M. H., and M. Kanamitsu, 1994: The NMC nested regional spectral model. *Mon. Wea. Rev.*, **122,** 3–26.

Machenhauer, B., 1979: The spectral method. *Numerical Methods Used in Atmospheric Models*, Vol. II, GARP Publication Series, No. 17, GARP/WMO-ICSU Joint Organizing Committee, 121–275.

Miller, M. J., and A. J. Thorpe, 1981: Radiation conditions for the lateral boundaries of limited-area numerical models. *Quart. J. Roy. Meteor. Soc.*, **107,** 615–628.

Miyakoda, K., and A. Rosati, 1977: One-way nested grid models: The interface conditions and the numerical accuracy. *Mon. Wea. Rev.*, **105,** 1092–1107.

Ooyama, K. V., 1987: Scale-controlled objective analysis. *Mon. Wea. Rev.*, **115,** 2479–2506.

——, 2001: A dynamic and thermodynamic foundation for modeling the moist atmosphere with parameterized microphysics. *J. Atmos. Sci.*, **58,** 2073–2102.

Orlanski, I., 1976: A simple boundary condition for unbounded hyperbolic flows. *J. Comput. Phys.*, **21,** 251–269.

Orszag, S. A., 1970: Transform method for calculation of vector-coupled sums: Application to the spectral form of the vorticity equation. *J. Atmos. Sci.*, **27,** 890–895.

Phillips, N. A., and J. Shukla, 1973: On the strategy of combining coarse and fine grid meshes in numerical weather prediction. *J. Appl. Meteor.*, **12,** 763–770.

Shapiro, L. J., and K. V. Ooyama, 1990: Barotropic vortex evolution on a beta plane. *J. Atmos. Sci.*, **47,** 170–187.

Staniforth, A., and J. Côté, 1991: Semi-Lagrangian integration schemes for atmospheric models—A review. *Mon. Wea. Rev.*, **119,** 2206–2223.

Straka, J. M., and J. R. Anderson, 1993: Extension and application of a local, minimum aliasing method to multidimensional problems in limited-area domains. *Mon. Wea. Rev.*, **121,** 2903–2918.

Zhang, D.-L., H.-R. Chang, N. L. Seaman, T. T. Warner, and J. M. Fritsch, 1986: A two-way interactive nesting procedure with variable terrain resolution. *Mon. Wea. Rev.*, **114,** 1330–1339.